

Fluid-driven hydrovolcanic activity along fracture zones and near seamounts: Evidence from deep-sea Fe-rich spherules, Central Indian Ocean Basin

Ankeeta Amonkar^{1, 2*}, Sridhar D. Iyer³, E.V.S.S.K. Babu⁴, N. Shailajha⁵, Areef Sardar¹, and S. Manju⁴

¹CSIR-National Institute of Oceanography, Dona Paula, Goa 403004, India

²Marine Science, School of Earth, Ocean and Atmospheric Sciences, Goa University, Goa 403206, India

³Formerly with CSIR-National Institute of Oceanography, Dona Paula, Goa 403004, India

⁴CSIR-National Geophysical Research Institute, Hyderabad, Telangana, 500007, India ⁵Department of Earth Science, Pondicherry University, Pondicherry 605014, India

(*corresponding author aamonkar@nio.org; ankeetaamonkar9@gmail.com)

Abstract

An insight on occurrence of Fe-rich spherules from the Central Indian Ocean Basin (CIOB) provides an understanding of their distribution at a water depth of >5,000 m. In the present study, Fe-rich spherules are identified to occur in two different sediment types (i.e., siliceous and pelagic) and tectonic settings (i.e. near seamounts and fracture zones). These are single spheres or aggregates, of different sizes (63 to 390 μm) and show textural variability (smooth/quenched, brickwork, corkscrew, interlocking and dendritic). A comparative study based on physical morphology and chemical composition suggests a common mechanism of formation.

The association of spherules with FZ and seamounts signifies that morpho-tectonic features play an important role in fluid-driven hydrovolcanism. Based on the evidence and geologic conditions existing in the basin, we conclude that molten fuel-coolant interaction (MFCI) coupled with submarine hydrothermal exhalations could be an ideal mechanism for the formation of spherules and Fe-particles. The accretion of the spherules on the surface sediments could be a result of recent volcanic phenomena, while those occurring at different depths (280-355, and 460-475 cm-bsf) within the sediment core indicate two different episodes. The study provides a global implication in understanding fluid-driven magmatism in a deep-sea intraplate environment.

Keywords: Fe-rich Spherules, Deep-sea sediments, CIOB, Hydrovolcanic activity

1.0 Introduction

The first report of black magnetic spherules from the deep-sea sediments of the Pacific Ocean dates back to the HMS Challenger Expedition in 1876 by Sir John Murray (Patterson and Fredriksson, 1958). Later, opaque magnetic and metallic spherules were reported from ferromanganese (FeMn) nodules from the Pacific Ocean (Murray and Renard, 1891). After a lull of a few decades, a series of reports concerning such spherules were published. For example, spherules occurring in ferromanganese crusts at 45°N on the Mid-Atlantic Ridge (MAR; Aumento and Mitchell, 1975), limestones and carbonates (Freeman, 1986; Suk et al., 1990), lunar soils (Heiken et al., 1974), extraterrestrial materials (El Goresy and Fechtig, 1967, Szoor et al., 2001) and tektites (Kleinman, 1969). Recently, occurrence of magnetite spherules was reported from a thin ferruginous layer of Fatehgarh formation (Cretaceous) of Barmer Basin, India (Mathur et al., 2019).

Till the last few decades, metallic spherules of similar morphology and chemical composition to the cosmic spherules were misleading. The origin of metallic spherules with a lesser meteoritic abundance of Ni and an appreciable Mn were enigmatic to explain (El Goresy and Fechtig, 1967; El Goresy, 1968). Subsequently, it was shown that spherules with an absence of Ni core and enhanced Si were derived from volcanic sources (Finkelman, 1970).

To-date, spherules have been identified to be composed of single or composite minerals such as silicate (Lefevre et al., 1986), K-feldspar and glauconite (Nashlund et al., 1986), phosphatic conodont pearls (Wang and Chatterton, 1993) and aluminium-rich spherules (Shterenberg et al., 1986; Dekov et al., 1995; Iyer et al., 2007) or may be of basaltic composition (Melson et al., 1988; Robin et al., 1996). Different sources/processes have been proposed for their formations such as volcanism (dominant source), while other sources include anthropogenic, biogenic activity, sedimentary processes, cosmic dust, and extra-terrestrial impact and from modern industrial processes (Zagurskii et al., 2009; Huang and Xu, 2012; Shetye et al., 2019).

The occurrence of spherules in diverse geological environments has led to a wide application (Wang and Chatterton, 1993; Ma and Bai, 2002). Spherules are used as stratigraphic markers to infer palaeo-environmental conditions and geological events. This is evident from the occurrence of spherules between the strata of major geological events such as the extra-terrestrial impact during the Permian–Triassic and K-T times (Alvarez et al., 1992; Parthasarathy et al., 2019), the Precambrian–Cambrian, Early-Middle Cambrian, Frasnian–Famennian, Permian–Triassic, Callovian–Oxfordian and Maastrichtian–Danian boundary intervals (Zhang et al., 2010; Glass and Simonson, 2012; Huang and

Gong, 2014; Zhang et al., 2014; Chang et al., 2017) and in Mesozoic-Cenozoic deposits from the Atlantic Ocean (Lozovaya, 1981).

Harrison and Peterson (1965) reported the occurrence of an unusual abundance of a highly magnetic mineral in a sediment core recovered from the Indian Ocean (23°56'S and 73°53'E; water depth of 3,676 m). According to those authors, the mineral was maghemite with some aspects of magnetite. Perhaps this was the first report of Fe-rich spherules in the Indian Ocean. Later, Iyer et al. (1997a, b; 1999a, b) reported the presence of magnetite spherules from two different sites in the Central Indian Ocean Basin (CIOB): one at the base of an intraplate seamount located in siliceous sediments and other along the Triple Junction Trace in the Indian Ocean (TJT-In). Apart from the above report, so far there is not much work concerning the deep-sea spherules to understand their distribution and formation.

In the above background, we report the distribution of Fe-rich spherules recovered from a water depth of ~5,000 m from the CIOB. We have classified the spherules based on their occurrence, physical parameters, and chemical compositions. The spherules in the surface and core sediments were exclusively sampled from and/or near morpho-tectonic features such as fracture zones (FZ) and seamount clustered areas. We have compared the variability in the size, texture, and composition of the spherules with those reported earlier from the CIOB, Pacific and Atlantic oceans and also with experimentally produced spherules. Finally, a plausible mechanism for the formation of spherules is proposed which could be applicable to the occurrence in the world ocean giving this work a wider application in understanding fluid-driven magmatism in a deep-sea intraplate environment.

2.0 Study Area

The CIOB is located in an intraplate environment and extends from latitudes 6°S to 20°S and longitudes 72°E to 80°E and has an average water depth of 5,000 m (Mukhopadhyay et al., 2018). Based on detailed bathymetric surveys, Kodagali et al. (1992) divided the basin into three regions: high, plain and medium relief areas, moving from west to east of the basin. The FZ (73°E, 75°E, 79°E, 83°E, and 85°E), triple junction trace (76.5°E) faults, lineations, and hundreds of seamounts and abyssal hills all form major morpho-tectonic features in the basin (Das et al., 2005, 2007).

Due to its wide lateral extent, the CIOB has a significant effect on sediment distribution, composition and lithofacies. Siliceous sediments dominate in the central region while red-clay occurs below 15°S. The occurrence of carbonate preservation in calcareous sediment over a seamount summit has also been reported (Nath et al., 2012). Ferromanganese (FeMn) nodules and crusts that

are closely associated with siliceous sediments, forming economically potential deposits (Mukhopadhyay et al., 2018).

Preliminary observations of the Fe-rich spherules gave a firsthand understanding on the distribution of spherules on the CIOB seafloor. In the present study, we have targeted two different tectonic settings (seamounts and FZ) and sediment types (siliceous and pelagic) to obtain better understanding on spread and genesis of Fe-rich spherules in the deep-sea environment. Due to availability of detailed geophysical data, the 79°E FZ was selected for sampling. Sediment cores were retrieved adjacent to the FZ from both the domains (siliceous and pelagic). We now discuss the geological setting of both the sampled sites in details.

2.1 Geological setting of Seamounts (Site-1)

In the CIOB seamounts between 10°S and 14°S occur as isolated entities or in chains that are aligned N-S while some seamounts that are associated with FZ and have E-W elongated base. This was inferred to be due to addition of magmatic mass from subsequent eruptions along FZ and indicated multiple volcanic episodes (Das et al., 2007). This is borne out by the occurrence of relatively fresh basalts on the seamounts, compared to the surrounding seafloor and suggests volcanism to have been active even after the emplacement of seamount that took place several million years ago (Iyer et al., 2018).

2.2 Geological setting of Fracture Zone (Site-2)

The 79°E FZ also known as Indrani FZ (Indrani or L'Astrolabe), originated from the Southeast Indian Ridge (SEIR), and traces of which are observed on either side of the ridge. Geophysical data of this FZ indicate a ridge and trough topography. Further, it is observed that during magnetic anomaly A26 to A21 the Indian Plate underwent a change in direction during the global plate reorganization in the Indian Ocean (Dyment, 1993; Yatheesh et al., 2019). The 79°E FZ has a throw of 100 m to the east (Kamesh Raju et al., 1993) and there are several seamounts at its southern end (Das et al., 2007). Some of these seamounts show additions of magmatic material post formation (Iyer et al., 2018).

2.3 Sampling sites

The sediment samples used for this study were retrieved during various cruises carried out as a part of the on-going “Surveys for Polymetallic Nodules” project. The samples retrieved from the above described geological settings (**Fig. 1A**), are discussed below.

In the year 2001, a total of fifty five (55) stations were sampled on research vessel A.A. Sidorenko (Cruise #38). The sediments were retrieved using an Okean grab that also brought up FeMn nodules (**Table 1A**). The samples were collected in a close grid pattern within the coordinates of 10.25°S to 12.75°S and 74°E to 76°E (**Fig. 1B**).

Site-1 (*Seamount clustered area*): During the 48th expedition of RV Sindhu Sadhana in April 2018, forty (40) surface sediment samples were collected using an Okean grab from the abyssal plain in the vicinity of seamounts and from seamount clustered area (**Fig. 1A and B**) (**Table 1B**).

Site-2 (*Near fracture zone*): During the 22nd cruise of RV A.A. Sidorenko in the year 1999, two (2) gravity cores (5m long) were recovered adjacent to the 79°E FZ. The former core AAS-22/7 was from the siliceous sediments (10°S and 78°E, water depth 5,240 m) while, core AAS-22/3 was from the pelagic sediments (16° 59' S and 77° 59' E, water depth 4,760 m; **Fig. 1A**).

3.0 Methodology

As it was vital to understand the distribution of black magnetic spherules, sampling of the seafloor was carried using a powerful magnet attached to the Okean grab (at 55 stations on AAS-38). The two gravity cores were sub-sectioned at 5-cm interval in order to study the downcore variation of the coarse fractions (CF) and distribution of Fe-rich spherules. The sub-sectioned core sediments were oven-dried at 60-70°C to remove water content. About 25 g each of the sample was treated with 20 ml of 10% of Na-hexametaphosphate, kept overnight to disperse the clay and subsequently wet sieved using 63µm mesh. The CF recovered after sieving was again oven-dried and prepared for further examination. The percentage of CF was calculated based on the recovered fraction subtracted by the loss of dry sediment. In addition, several kilograms of sediment collected using spade corers were sieved on board and the magnetic fractions were separated using a hand-held magnet (processed on board RV Sindhu Sadhana, cruise no. 48). The abundance of spherules per 100 gm of the dry sediment was calculated for core samples from Site-2.

3.1 Analytical Procedures

From the CF, magnetic fractions were separated using a hand bar magnet and observed under an OLYMPUS SZX7 binocular microscope. Spherules and co-occurring magnetic particles were hand-picked, mounted on a plastic stub and carbon. The surface features were identified using a JEOL-5800LV scanning electron microscope (SEM). The working distance was 20 mm and the accelerating voltage was 20 kV with a dead time of 20%.

The major oxide data of the Fe-rich spherules were obtained using an Energy Dispersive Spectrometer (EDS; OXFORD ISIS) attached to an SEMat CSIR-National Institute of Oceanography and a Cameca SX 100 Electron Probe Micro Analyser (EPMA) at CSIR-National Geophysical Research Institute, Hyderabad. During EDS analysis, the working distance was 12 mm, counting time was 100 sec, counting rate varied between 1,500 and 3,000 cps and the dead time was below 20%. The mineral standards (albite and orthoclase) were used during the analysis to check the accuracy which was noted to be less than 2%.

The operating conditions for EPMA were 20kV accelerating voltage, 5 μ m beam diameter and 20nA beam current. All the elements were analysed sequentially using wavelength dispersive spectrometry (WDS). To improve the quality of some low abundance elements (Si, Na, K, Ti and Mn), analytical strategy of integrating data from the analysis on more than one spectrometer was used. This resulted in <0.5% error for the major elements. Native Fe standard was used during the analysis and the accuracy of the data was better than $\pm 0.4\%$. The data were cross-checked with Fe₂O₃, Andradite and FeS₂ standards to confirm the quantification. ZAF corrections were incorporated before finalizing the data.

4.0 Results and Interpretations

Distribution map of CIOB spherules was made using data from the 55 stations located above Site-1 (data are depicted in **Fig. 2**). Based on this data, the sampling sites were selected. The details of the sediment samples and coarse fraction are now discussed.

4.1 Sediment characteristics and coarse fraction description

The 40 surface samples from Site-1, are pale yellow to light brown in colour and have a silty texture. The northern core (AAS-22/7), retrieved from the siliceous domain (Site-2) has yellowish-brown colour sediment with silty-clayey texture while the southern core (AAS-22/3) from pelagic clay has dark brown sediment with clayey appearance and is slightly compact. Further, it was noted that in the core AAS-22/7, the sediments associated with the Fe-rich spherules had a slightly darker color (**Fig. 3**).

The graph of CF% vs. core depth (**Fig. 4**) shows considerable variations in both the cores. In the northern core AAS-22/7, CF% abruptly changed from 5 to 10% with prominent peak (nearly 13%) occurring at depths of 285 and 355 cm-bsf (below seafloor). While in the southern core AAS-22/3, the CF% was high only in the top 35 cm and below 35 cm-bsf there was a relative decrease (2-3%). In general, the CF from Site-2 revealed an assemblage of components such as radiolarians, Fe-Mn micronodules, basaltic glass, palagonite grains, volcanic glass shards, microtektites, pumice

pieces, bread crust (oxidized basaltic glass), magnetic spherules, mica flakes and phillipsite crystals (Amonkar and Iyer, 2017; Amonkar et al., 2020). While, the detailed examination of CF (>63 µm) from Site-1 revealed the occurrence of FeMn micronodules, radiolarians and diatoms as the dominant phase together with spherules and volcanic glass shards. However, this study only emphasizes on the Fe-rich spherules and associated Fe-rich particles in CIOB.

4.2 Fe-rich Spherules

4.2.1 Spatial and temporal distribution

The data obtained from 55 sediment locations (**Table 1A**) indicate the bulk Fe-rich spherules present in the CF. We observed a high abundance of spherules in the area between 10.3°S and 11°S with the number of spherules ranging from 400 to 996 (**Fig. 2**). These locations when traced on a bathymetric map showed the existence of a seamount and FZ adjacent to the sampled Site-1 (**Fig. 1B**).

The Fe-rich spherules collected from Site-1 were noted to be varying in few hundred while; those occurring at Site-2 were manually counted. The abundance of spherules in the top section i.e. up to 5 cm-bsf (AAS-22/7) and in the top 10 cm-bsf (AAS-22/3) was observed to be 180-200/100g of dry sediment. Apart from this, abundant spherules were noted to occur at two distinct depths i.e. 280-355, and 460-475 cm-bsf in the core AAS-22/7 (**Fig. 4**). The abundance of spherules at depth 280-355 and 460-475 cm-bsf was noted to be 280-440/100g and 280-320/100g respectively. Here it was interesting to note that the intermediate depth (280-355 cm-bsf) with the highest number of spherules occurred within the baked sediments (**Fig. 3**) and were associated with volcanogenic-hydrothermal materials (vhm) and basaltic materials.

4.2.2 Physical characteristics: Shape, size and texture

In general, the spherules under the binocular microscope appear as tiny spheres that adhere to one another by weak magnetic forces. The spherules have a metallic lustre and are dark grey to mostly black while a few are reddish-brown in colour. Most of the spherules are smooth while a few have an uneven surface because of additional material in the form of fragile aggregates. A total of 77 spherules were observed under an SEM of which 38 spherules from Site-1 (**Table 2.1**) and 39 spherules from Site-2 (**Table 2.2**) have been detailed with respect to shape, size, texture and chemical composition.

The spherules largely appeared to be spherical under a binocular microscope but a detail observation under SEM revealed five major shapes. These are spherical, broken, teardrop, unevenly spherical and oval. Based on these observations, we have classified the spherules occurring at both sites (**Tables 2.1 and 2.2**). At Site-1, the spherules are mainly spherical (34) with a few broken (3)

and teardrop (1), while those at Site-2 are spherical (25), non-spherical (9) and oval (5). Overall, spherical shaped spherules are relatively more at Site-1 than at Site-2.

However, out of the total 77 spherules studied from both the locations, 59 spherules (77%) were spherical, 9 spherules (12%) were non-spherical, 3 were broken (4%), 1 had a teardrop morphology (1%) while the remaining 5 spherules (6%) were oval in shape (**Fig. 5A**). A few of the spherical spherules had a bulge and mould-like protrusion with an incipient tail-like feature. Apart from all above, we also observed Fe-rich particles that were attached to some of the spherules which will be discussed below. In general, the size of the spherules ranges from 63 to 390 μm . The spherules from the study area were classified based on three major size ranges (63-125, 126-220, and $>220 \mu\text{m}$). The size classification data indicate that 30 spherules (41%) fall in the range of 63-125 μm and 35 (47%) are 126-220 μm while 9 (12%) are $>220 \mu\text{m}$ (**Fig. 5B**).

Based on the textures, we have classified the CIOB spherules into two types: smooth spherules with no crystallinity (**Fig. 6**) and spherules with well-defined crystals that are arranged in different geometrical patterns (**Fig. 7**). Most of the CIOB spherules appear smooth (**Figs. 6a and 6b**) while on some smooth textured spherules, there are aggregates of minerals resulting in a slightly uneven texture (**Figs. 6c and 6d**). Apart from these, we observed some spherules to have protrusions at their end (**Fig. 6e**), a few were fused (**Fig. 6f**) while broken (**Figs. 6g and 6h**) spherules are quite uncommon. On the other hand, the crystallized spherules are classified into brickwork (**Figs. 7a and 7b**), corkscrew (**Fig. 7c**), interlocking (**Fig. 7d**) and dendritic (**Figs. 7e and 7f**). Blowholes (**Fig. 7g**) occurring on the surface of the spherules were circular to lenticular in shape and were mainly observed between two larger crystals. Apart from all these textural varieties, we observed a few grains, adhered to the spherules, and these were well-crystallized with cubic symmetry and a metallic lustre (**Fig. 7h**).

The presence of surface textures, blowholes and mineral aggregates as described above, led to the inquisitiveness about the internal structure. Hence, we examined 14 polished spherules to understand the continuity of the surface textures and presence of mineral inclusions (if any) inside the spherules. It was seen that the textures identified above were only on the surface and continued a few microns inwards. The internal surface showed massive aggregates (**Fig. 8A**) and in a few spherules, small crystals are observed in a smooth matrix (**Fig. 8B**). Additionally, continuity of the blowholes was noted in the interior of the spherules (**Fig. 8C and 8D**) and in some spherules the blowholes get widened towards the inside of the spherules. In all the cases the blowholes are completely hollow (**Fig. 8E**). Apart from these features, some spherules are massive in the interior with no phase differentiation (**Figs. 8F, G and H**).

4.2.3 Chemical composition

The major oxides obtained for 57 non-polished spherules and 11 polished spherules from the two sampled sites are shown in **Tables 3A and 3B** and the minor elements in **Table 3C**.

The 31 unpolished spherules analyzed from Site-1 consist of an extremely high amount of Fe along with insignificant amounts of Si, Al, Mn, Mg, Ca, K, N, and Ti (**Table 3A**) while S, Cr, Zn, and Ni (**Table 3C**) occur in minor amount. The Fe content ranges from 62 to 87 wt.% with spherules (sample S-S4) having significantly higher Fe (87 wt.%). Si ranges from 0.2-2.5 wt.%, Al 0.3-4.6 wt.%, and Mn 0.4-1.5 wt.%. Similarly, K was observed in samples S-S5 (2.6 wt.%) and in S-KS2 (4.6 wt.%). Ca, Mg and Na were also observed to be very low (< 3 wt.%). Ti was present only in spherule sample S-K3S5 (0.8 wt.%). The 26 unpolished spherules analyzed from Site-2 showed a similar elemental distribution. Fe was noted to range from 68 to 77 with the lowest content in spherule sample F-S47-2 (60 wt.%). Si 0.09-2 wt.%, Mn 0.3-1.8 wt.% and Al 0.2-0.8 wt.% while K, Mg, Ca and Na were less than 5 wt.%. Though the concentration of Ti is very low (0.2 to 0.4 wt.%) yet it was noted to be in more spherules from Site-2 as compared to the spherules at Site-1. Spherule F-S46 had the highest concentration of Ti (0.95 wt.%) while spherule F-S47-2 had an exceptionally higher Na (4.7 wt.%). The averages calculated for spherules occurring in both the studied sites indicate that the spherules near the Indrani FZ (Site-2) have a higher amount of Fe and Na while those near seamounts (Site-1), showing an enrichment in Si, Al, Mn, K, and Ca with values nearly two times more. The Fe content in the spherules of Site-1 was slightly lower than those at Site-2.

In addition to the major elements, we observed Cr, S, Zn, and Ni to be present in a few spherules (**Table 3C**). In general, Cr ranges from 0.17 to 0.99 wt.%, S (0.11 to 1.68 wt.%), Zn (0.31 to 0.56 wt.%) with an exception in spherule S-KS3 (3.57 wt.%) and highest (6.34 wt.%) in F-S31-1. Ni was between 2.67 and 7.79 wt.%. The spherules from Site-1 have a notable amount of Ni along with Zn and S while those at Site-2 have more Cr. These elements mostly occur in the FeMn oxides that partially coat the spherules. Microprobe analysis (from core to rim) of 11 polished spherules for major and trace elements shows a strong variance compared (i.e., low contents of Si, Al, Ti, Mn, K, and Mg) to the unpolished ones (**Table 4**). The interior of the spherule has extremely high Fe value (>98 wt.%) compared to the surface. The compositional data show Si to be very low (<0.02 wt.%) except in one of the spherules where it is slightly higher (0.6 wt.%). The Ti values range up to 0.06 wt.% while Al varies between 0.02 and 0.08 wt.%. Ca, Na, K, and P show a range up to 0.02 wt.% while Mn and Mg are between 0.2 and 0.8 wt.%, and 0.01 and 0.04 wt.%, respectively. The significantly low amount of Ni (<0.06 wt.%) clearly signifies that the spherules are not derived from extraterrestrial sources. There are discrete areas (**Fig. 8**) with high Fe values (>98 wt.%) in a silicate

matrix. In summary, compositions of the polished surface from core to rim (**Table 4**) do not show any significant changes. It appears that the specimens are native iron spheres that dispersed in the CIOB sediments. Based on the detailed physical and chemical observation, we infer that the CIOB spherules, despite their variable size (**Fig. 5**), wide range of textures (**Figs. 6 and 7**) and a narrow range in elemental distribution (**Tables 3A and 3B**), and must have formed by a similar process. The presence of Si and other elements together with S in appreciable amounts reaffirms the CIOB spherules to be volcanic in origin.

4.3 Fe-rich Particles: Physical and chemical parameters

Fine magnetic particles and basaltic glass that are cm-sized co-occurred with Fe-rich spherules and were attached by weak magnetic force. These fragile and uneven particles under the binocular microscope are reddish-brown to dark red in colour and some are nearly black. Under the SEM, these particles portray a fine granular texture (**Fig.9**).

The SEM-EDS data of the Fe-rich particles are presented in **Table 5** along with their average values and standard deviation. In these Fe-rich particles, Fe ranges from 59 to 74wt.%, while Al (0.4-2wt.%), Ti (2-8wt.%), Mg (1-1.8wt.%), Ca (0.2-0.4wt.%) and Mn (0.6-0.8wt.%) contents were very low. Similar to the spherules, these Fe-rich particles also contain a significant amount of Ba, Cr, S, Zn, and Cu and P, V, and Pb in minor amounts. The Fe content of these associated particles is relatively lesser than those in the observed spherules (62 to 87wt.%). Si is low (0.19-1.06wt.%) and shows an inverse relation with Fe. Ti is high (6.45 to 12wt.%) with the exception of samples 28-1 and 32-2 (2-0 to 2-2wt.%). There are also particles with moderate Fe (47wt.%) and high Si (4.8wt.%) and Ti (12wt.%) and well-developed cubic form (**Fig.6P**). These particles were identified to be a titanomagnetite crystal. Overall the fine magnetic particles are mainly Fe-Ti rich with low silica. The Fe-rich particles co-existing with the spherules suggest that they too must have formed by a common process.

4.4 Comparison with other Fe-rich spherules

In order to understand the origin of the CIOB Fe-rich spherules, we have compared their chemical compositions with similar spherules reported earlier from the basin (**Table 6**). Our present data show a remarkable similarity with the spherules recovered at stations SS2/94, SS2/89, and SS10/657 in the CIOB (Iyer et al., 1997a, b; 1999). But in our spherules, there is a relative enrichment of Mg, Mn, Ca, K, and Na along with Cr and Ni. The Ti value of Site-2 is similar to those of SS2/89 and SS10/657 (Iyer et al., 1997a), while the site-1 has significantly higher Ti (0.80 wt.%). Si, Al and Ca values from Site-2 (FZ) are akin to those reported earlier unlike the spherules at

Site-1 (seamounts). Ti shows an inverse relation with Fe for spherules from the Sites (1 and 2), Fe particles and those previously reported from the CIOB. But overall the chemical data of spherules from the present study are in the range with the reported ones from sites SS2/94, SS2/89, and SS10/657 (Iyer 1997a, b; 1999).

When compared with the Fe-rich spherules from Mt. Etna, Mt. Lipari, Mt. Vesuvius, Mt. Bracciano (Del Monte et al., 1975), we observed a similar distribution of Fe but not for the other elements that co-occur in the spherules (**Table 6, Sr No. 7-10**). The spherules from the MAR resemble those from the CIOB but the former have less Fe content. We observed that the CIOB Fe-rich spherules do not compare well with the basaltic spherules from DSDP Site 32, NE Pacific Ocean (Melson et al., 1988). Neither with experimentally produced large Fe-Al, small Fe-Al, blocky Fe particles, and droplets of basaltic glass of Kilauea Iki, Hawaii (Heiken and Wohletz, 1985), basaltic hydromagmatic ash (Wohletz and McQueen, 1984), and basaltic microlapilli from the Vityaz FZ, Indian Ocean (Nath and Iyer, 1989). The Fe content was very low in all of these reported materials and thus indicates that the process of formation could be quite different for the CIOB spherules.

5. Discussion

Since a long time the origin of deep-sea spherules has been a subject that has been less explored and debated. This is mainly because such spherules were considered to be melted terrestrial material that was ejected during the impact of the extra-terrestrial body on earth (Wright and Hodge, 1965; Glass and Simonson, 2012; Reshma et al., 2013). However, with experimental understanding of spherule formation (Peckover et al., 1973, Sheridan and Wohletz 1981; Wohletz et al., 1995; White 1996), it was quite clear that the spherules could also be a product of volcanism. Volcanically derived Fe-rich spherules are easily identified by their surface appearance and presence of magmaphile elements. In contrast, cosmic spherules have a distinct etched surface, barred texture and Ni-rich core (Finkelman, 1970; Heiken and Wohletz, 1985; Prasad et al., 2015).

The observations carried out on 77 spherules from both the sites in the CIOB (34 occurring at Site-1 and 25 at Site-2) suggested, spherical spherules to be dominant with a few of uneven or oval shape (**Tables 2.1 and 2.2**). Five major shapes identified in the present study are similar to those reported earlier for the CIOB. The spherules varies from 63 to 390 μm but mostly range from 126 to 220 μm (**Fig. 5B**) making our observation corroborate well with previously reported sizes ($<475 \mu\text{m}$) (Iyer et al., 1999).

The textural classification accounted in the present study has largely helped to distinguish crypto-crystalline (smooth-surfaced) and crystalline spherules. Spherules with smooth surface texture

would have probably formed by a process of quenching of hot lava that had very little time for the growth of crystals and therefore crystals are either absent or minute in size (cryptocrystalline) (**Fig. 6**). On the other hand, the well-textured spherules suggest a slow cooling of the lava (**Fig.7**). Blow holes are quite common in most of the spherules and these possibly developed during the escape of volatiles from within the spherules (Iyer et al., 1999).

The spatial distribution study indicates a higher abundance of spherules in the areas associated with seamounts and FZ. This implies that morphological parameters occurring at Site-1 i.e. seamounts and FZ (**Fig. 1B**) may be an active regime for localized volcanic activity which may have produced these spherules. The possibility of these Fe-rich spherules to be of recent origin cannot be ruled out as these are associated with surface sediments. The occurrence of spherules (180-200 spherules/100g) in the surface sediments of both the gravity cores retrieved adjacent to the 79°E FZ also supports the possibility of a recent hydrovolcanism in CIOB.

The temporal distribution study carried on gravity cores suggest two major events occurring at core depth 280-355 and 460-475 cm-b.s.f. The association of spherules with basaltic material and vhm clearly indicates a hydrovolcanic origin. Further, detailed study on morphology and composition of spherules from Sites-1 and 2 do not display much difference. This fact implies that the process of formation of the CIOB spherules could be similar irrespective of the site at which these formed.

5.1 Formational Process of Fe-rich Spherules

The investigations of the CIOB spherules by Iyer et al. (1997a, b; 1999) ruled out several sources that could probably be the reasons for their occurrence in different sediment types and near morpho-tectonic features. The sources are sampling artefacts, industrial or anthropogenic contributions (cf. Puffer et al., 1980), terrestrial volcanic eruptions (cf. Fredrickson and Martin, 1963; Hodge and Wright, 1964; Wu et al., 2013), extra-terrestrial inputs (cf. Schmidt and Keil, 1966; Mutch, 1966), diagenetic (McCabe et al., 1983) and biological (Wang and Chatterton, 1993; Ma and Bai, 2002). Deep-sea spherules of cosmic origin have textures akin to volcanic spherules but the former have Ni-rich core (e.g. Finkelman, 1970; Genge et al., 2017) while the volcanically derived spherules contain magmaphile elements (Heiken and Wohletz, 1985). Based on such evidence Iyer et al. (1997 a,b) opined that the CIOB spherules were formed volcanically in an intraplate environment.

Considering several factors, we now discuss the likely processes that could result in the production of the CIOB spherules. These processes are submarine hydrothermal exhalations, fuel-coolant interaction (FCI) and molten fuel-coolant interaction (MFCI). The first proposed mechanism

for the formation of spherules was submarine hydrothermal exhalations. Harrison and Peterson (1965) suggested the role of hydrothermal exhalations and the release of CO₂ resulting in a change in temperature and pressure, thereby affecting the pH of the water column and enhancing the formation of the Fe-rich mineral phase in deep-sea sediments. This process was used to explain the unusual abundance of iron in the East Pacific Rise (Goldberg and Arrhenius, 1958), in-situ origin of a magnetic mineral near abyssal hills in the Indian Ocean (Harrison and Peterson, 1965), the Amorphous Goethite Facies of the Red Sea metalliferous sediments (Bischoff, 1969), microscopic amorphous iron-manganese oxide precipitates (0.5 to 25 μm) in the sediment columns near the Mendocino and Murray FZ (von der Borch and Rex, 1970) and formation of modern iron spherules in Panarea volcanic island of Aeolian Arc (Bella et al., 2019).

Later, Peckover et al. (1973), Sheridan and Wohletz (1981), Wohletz and McQueen, (1984b), and Wohletz et al. (1995) experimentally demonstrated that during hydrovolcanic eruptions a mechanism that resembles 'fuel-coolant interaction' (FCI) takes place. During such a process an explosion is caused by rapid vaporization of water during its contact with molten material. This phenomenon of rapid vaporization of water is also noted in metal processing and foundry industries. Wohletz (1983) reported that when a hot magma is exposed to cold seawater, it results in the mixing of the two melts before explosion. Fragmentations of the mixture in such cases supposedly increase the contact area of melt and water resulting in an enhanced conductive heat exchange at the site of the explosion.

Wohletz and McQueen (1984b) mixed thermite (Al + Fe₂O₃) (equivalent to basalt) and quartzo-feldspathic material (akin to siliceous sediment) and water in a steel container and this mixture was blown at high pressure. The spherules thus formed were of different shapes and sizes and with variable Fe, Si and Al contents.

The third mechanism (MFCI), is a refinement of the FCI with molten melt as an additional parameter. Zimanowski et al. (1995, 1997) opined that MFCI takes place in four phases. The hydrodynamic mixing phase, trigger phase, fine fragmentation phase, and finally vaporization and expansion phase. In the early stage, the process is initiated with hydrodynamic mixing of water and magma over a considerable time period. Those authors found that even in a reduced state the magmatic melt that is dispersed within the water will effectively allow solidification of melt in less than 1 second. Based on an experiment with a basaltic melt with ideal and close conditions, the authors reported that the resultant particles were of three shapes: (1) most abundant spherical particles that were perfectly rounded, (2) elongated and cylindrical particles, and (3) angular particles with pitted and cracked surface.

In the CIOB the presence of siliceous and pelagic sediments, occurrence of MORB (on the seafloor and at seamounts) (Das et al., 2007; Iyer et al., 2018), and hydrothermal material at sites SS2/89, SS10/657 and SS2/94 (**Fig. 1**) (Iyer et al., 1997a, b; 1999b); all of these indicate a condition similar to the field experiments discussed above. We propose a model (**Fig. 10**) in which MFCI together with submarine hydrothermal exhalations may have led to the formation of the Fe-rich spherules.

During hydrovolcanic activity a hot Fe-rich melt perhaps seeped from minor fractures and fissures present either near/close to seamounts and/or FZ. During this activity there could be MFCI coupled with hydrovolcanic activity that resulted in rapid quenching of molten material due to interaction with cold seawater and this must have consequently resulted in Fe-rich spherules and particles of variable shapes, sizes, and textures in the CIOB. Further, the occurrence of basaltic material along with Fe-rich spherules and particles at two different core depths (280-355, and 460-475 cm-bsf) in the core AAS-22/7 indicates two magmatic events. This could be driven by lateral (horizontal) movement of the magmatic fluid from the fissures and cracks occurring near FZ and seamounts. The physical observation of dark sediments at these depths further confirms our finding. We suggest the present study area, composed of fissures and fractures that developed at the base of the seamount (Site-1) and FZ on the abyssal plain (Site-2) could be sites for hydrovolcanic activity (**Fig. 10**). Apparently, there are also sites in the CIOB where active Fe-rich fluids emanations are common, as previously proposed (Iyer et al., 1997a, b; 1999).

5.2 Volcanic-hydrothermal activities in the CIOB

The presence of a large volcanic province in the CIOB is attested by the extensive occurrence of basalts, spilites, pumice and glass shards that are of 60 Ma to recent times (Iyer and Sudhakar, 1995). In addition, there are hydrothermal signatures present on FeMn crusts occurring near 76°30'E FZ (Iyer, 1991) and on FeMn coated pumice (Kalangutkar et al., 2015). The hydrothermal activities that occurred near seamounts range in age from 625 to 10 ka (Iyer et al., 1997a, 1999). A younger hydrothermal event of ~100 yr was reported by Nath et al. (2008) based on ^{210}Pb , ^{238}U - ^{230}Th , ^{10}Be , major and trace elements, morphological and chemical data of sediments from the flank of a seamount occurring at 75.30°E FZ. In addition to these, hydrothermal events corresponding to ~7.5-9 Ma and 0.5 Ma were noted at ODP Sites 717-719 (Boulegue and Mariotti, 1990) (**Fig. 1**) while the formation of humic acid coupled with hydro-thermogenesis at 1°59.8'S/80°E, just below the same site (Sarma et al., 2017).

The above observations corroborate our present findings and suggest that channelized hydrothermal-volcanic activities in the CIOB may not be uncommon near the seamounts and FZ. These sites could be potential areas where vhm could form in a sub-seafloor environment. In addition, such events, albeit sporadic in nature, produced metal-enriched particles in the seafloor sediments (Amonkar, 2019).

6.0 Conclusions

This study is a comprehensive record of Fe-rich spherules from the CIOB. Sediment samples from two different sediment types (siliceous and red clay) and tectonic settings (seamount and FZ) provide a new understanding of the genesis of Fe-rich spherules and associated Fe-rich particles recovered from a water depth of 5,000 m. The Fe-rich spherules were categorized into five major shapes: spherical, broken, teardrop, unevenly spherical and oval. Textural studies indicate two major types of spherules: smooth quenched surface and well-crystallized magnetite that are arranged in different textural forms. The textures identified are brickwork, corkscrew, interlocking, and dendritic. The similarity in the chemical composition of Fe-rich spherules and associated Fe-rich particles from both the sites suggests that they were formed by a similar process. The spherules with lithophile elements and significant contents of S, Cr, Zn, and Ni suggest their hydrovolcanic origin on the seafloor.

Based on the observations and conditions prevailing in the basin, we conclude that MFCI coupled with submarine hydrothermal exhalations could be plausible processes for the production of spherules. The fluid-driven hydrovolcanic activity at a water depth of 5,000 m must have been controlled by morpho-tectonic features allowing the melt to circulate along these feeble plains. The circulating melt in contact with cold water must have either resulted in their quenching or produced well-crystallized Fe-rich spherules.

The occurrence of Fe-rich spherules within the surface sediments (Site-1 near seamounts) and in the top 10 cm-bsf in both the cores (Site-2 near FZ) suggests that the hydrovolcanic events may be of recent age. In contrast, the presence of Fe-rich spherules at two different core depths (280-355, and 460-475 cm-bsf) in the core AAS-22/7 indicates lateral seepage of a magmatic fluid. Based on the observations and regional outlook, we conclude that geological setting in the CIOB i.e. the seamounts and the FZ are potential sites for volcanic and hydrothermal activity in an intraplate environment.

Acknowledgements

We acknowledge the Director of CSIR-NIO, Goa for providing the facilities to carry out the study. We thank Dr.M. Shyam Prasad, retired scientist (CSIR-NIO), for sharing the data from which Fig. 2 was generated. We thank Charushila Desai and Tejas Salkar for help in preparing Fig. 1 and Fig. 10, respectively. The sediment samples were collected during several cruises (AAS-22, AAS-38 and SSD-48) under the auspices of the project “Surveys for Polymetallic Nodules” (GAP 2175) funded by the Ministry of Earth Sciences, New Delhi, India. This work forms a part of the doctoral work of AA and she thanks CSIR (Direct SRF) for the research grants. SN is grateful to Pondicherry University for allowing her to carry out Master’s degree (internship) at CSIR-NIO, Goa. We profusely thank the two anonymous reviewers for valuable comments which helped us to improve the manuscript. We are grateful to the Editor-in-Chief, Dr. Zengqian Hou and Dr. Fei Hong Cai, for encouraging us to re-submit the revised manuscript. We appreciate the help rendered by the Captains, crew, and participants of the many cruises during the sediment sampling operations. This is NIO’s contribution number (will be assigned on acceptance).

Conflict of Interest

We confirm that this work is original and has not been published elsewhere, nor is it currently under consideration for publication elsewhere. We have no conflicts of interest to disclose.

References

- Alvarez, W., Smit, J., Lowrie, Asaro, F., Margolis, S.V., Claeys, P., Kastner, M., and Hildebrand, A.R., 1992. Proximal impact deposits at the Cretaceous-Tertiary boundary in the Gulf of Mexico: A restudy of DSDP Leg 77 Sites 536 and 540. *Geology*, 20: 697-700.
- Amonkar, A., De Seixas, A., and Iyer, S D., 2017. Preliminary results of two sediment cores from the Central Indian Ocean Basin: Source of the coarse fractions. National Conference on Young Researchers, 16-17 March 2017, Goa University, Goa, India. (Poster).
- Amonkar, A., 2019. Metal-Enriched Particles in the Central Indian Ocean Basin: Characteristics, Composition, Origin and Possible Future Resource. Indian Science Congress Association, Lovely Professional University, Phagwara, Jalandhar, Punjab 3-7th Jan 2019.
- Amonkar, A., and Iyer, S. D., 2020. Extending the limit of widespread dispersed Toba volcanic glass shards and identification of new in-situ volcanic events in the Central Indian Ocean Basin. *Journal of Earth System Science* (Revised version submitted).
- Aumento, F., and Mitchell, W.S., 1975. Magnetic spherules from the Mid-Atlantic Ridge. *Geology*, 3: 407–410.

- Bella, M.D., Sabatino, G., Quartieri, S., Ferretti, A., Cavalazzi, B., Barbieri, R., Foucher, F., Messori, F. and Italiano, F., 2019. Modern iron ooids of hydrothermal origin as a proxy for ancient deposits. *Scientific Reports*, 9: 7107. <https://doi.org/10.1038/s41598-019-43181-y>.
- Bischoff, J.L., 1969. Red Sea geothermal brine deposits: their mineralogy, chemistry, and genesis. In: Degens, E.T., Ross, D.A. (Eds.), *Hot Brines and Recent Heavy Metal Deposits in the Red Sea*. Springer-Verlag, Berlin, 368–401.
- Blanchard, M.B., Brownlee, D.E., Bunch, T.E., Hodge, P.W., and Kyte, F.T., 1980. Meteoroid ablation spheres from deep-sea sediments. *Earth Planetary Science Letters*, 46: 178–190.
- Boulegue, J., and Mariotti, A., 1990. Carbonate cements and fluid circulation in intraplate deformation. In: Cochran, J.R., Stow, D.A.V., et al. (Eds.), *Proceedings Ocean Drilling Program, Scientific Results*, College Station, TX (Ocean Drilling Program), 116: 135–139.
- Chang, X-L., Hou, M-C., Liu, X-C., Orr, E., Deng, M., Chao, H., Wang, S., and Xiao, C., 2018. Abundant microspherules from the Upper Ordovician of northern Tarim Basin, Northwest China: Origin and palaeoenvironmental implications. *Geological Journal*, 53: 2,896–2,907. <https://doi.org/10.1002/gj.3128>.
- Das, P., Iyer, S.D., Kodagali, V.N., and Krishna, K.S., 2005. A new insight into the distribution and origin of seamounts in the Central Indian Ocean Basin. *Marine Geodesy*, 28: 259–269.
- Das, P., Iyer, S.D. and Kodagali, V.N., 2007. Morphological characteristics and emplacement mechanism of the seamounts in the Central Indian Ocean Basin. *Tectonophysics*, 443: 1–18.
- Del Monte, M., Nanni, T., and Tagliazucca, M., 1975. Ferromagnetic volcanic particulate matter and black magnetic spherules: a comparative study. *Journal of Geophysical Research*, 80: 1,880–1,884.
- Dekov, V.M., Mandova, E.D., Dimitrov, K.C., and Rekkalov, K.N., 1995. Native aluminium in metalliferous sediments from the East Pacific Rise axial zone (21°S). *Marine Geology*, 123: 87–103.
- Dyment, J., 1993. Evolution of Indian Ocean triple junction between 65 and 49 Ma (anomaly 28 to 21). *Journal of Geophysical Research*, 98: 13,863–13,878.
- El Goresy, A., 1968. Electron microprobe analysis and ore microscopic study of magnetite spherules and grains collected from the Greenland ice. *Contribution to Mineral Petroleum*, 17: 331–346.
- El Goresy, A., and Fechtig, H., 1967. Fusion crust of iron meteorites and mesosiderites and production of cosmic spherules. *Smithsonian Contribution, Astrophysics*, 11: 391–397.
- Finkelman, R.B., 1970. Magnetic particles extracted from manganese nodules: suggested origin from stony and iron meteorites. *Science*, 167: 982–984.
- Fredrickson, K., and Martin, L.R., 1963. The origin of black magnetic spherules found in Pacific island, deep-sea sediments, and Antarctic ice. *Geochimica et Cosmochimica Acta*, 27: 245–248.
- Freeman, R., 1986. Magnetic mineralogy of pelagic limestones. *Geophysical Journal International*, 85: 433–452. <https://doi.org/10.1111/j.1365-246X.1986.tb04522.x>

- Genge, M.J., Davies, B., Suttle, M.D., van Ginneken, M., and Tomkins, A.G., 2017. The mineralogy and petrology of I-type cosmic spherules: Implications for their sources, origins and identification in sedimentary rocks. *Geochimica et Cosmochimica Acta*, 218: 167–200.
- Glass, B. P., and Simonson, B. M., 2012. Distal impact ejecta layers: Spherules and more. *Elements*, 8: 43–48.
- Goldberg, E.D., and Arrhenius, G., 1958. Chemistry of Pacific pelagic sediments. *Geochimica et Cosmochimica Acta*, 13: 153–212.
- Harrison, C.G.A., and Peterson, M.N.A., 1965. A magnetic mineral from the Indian Ocean. *The American Mineralogist*, 50: 704–712.
- Heiken, G., and Wohletz, K.H., 1985. *Volcanic Ash*. University of California Press, Berkeley, CA, 246.
- Heiken, G., McKay, D.S., and Brown, R.W., 1974. Lunar deposits of possible pyroclastic origin. *Geochimica et Cosmochimica Acta*, 38: 1,703–1,718.
- Hodge, P.W., and Wright, F.W., 1964. Studies of particles for extraterrestrial origin. 2. A comparison of microscopic spherules of meteoritic and volcanic origin. *Journal of Geophysical Research*, 69: 2,449–2,454.
- Huang, C., and Gong, Y. M., 2014. Phosphatic microspherules and their geobiological implications from the Frasnian-Famennian transition at the Yangdi section, Guilin, South China. *Science China: Earth Sciences*, 57: 943–956.
- Huang, C., and Xu, R., 2012. Microspherules: Important information carriers bridging microscopic and cosmic worlds. *Earth Science-Journal of China University of Geosciences*, 34(S2): 97–116 (in Chinese with English abstract).
- Iyer, S. D., 1991. Comparison of internal features and microchemistry of ferromanganese crusts from the Central Indian Basin. *Geo-Marine Letters*, 11: 44–50.
- Iyer, S.D., and Sudhakar, M., 1995. Evidences for a large volcanic province in the Central Indian Ocean Basin. *Journal of Geological Society of India*, 46: 353–358.
- Iyer, S.D., Prasad, S.M., Gupta, S.M., and Charan, S.N., 1997a. Evidence for recent hydrothermal activity in the Central Indian Ocean Basin. *Deep-Sea Research-I*, 44: 1,167–1,184.
- Iyer, S.D., Prasad, S.M., Gupta, S.M., Charan, S.N., and Mukherjee, A.D., 1997b. Hydrovolcanic activity in the Central Indian Ocean Basin. Does nature mimic laboratory experiments? *Journal of Volcanology and Geothermal Research*, 78: 209–220.
- Iyer, S.D., Gupta, S.M., Charan, S.N., and Mills, O.P., 1999. Volcanogenic hydrothermal iron-rich materials from the southern part of the Central Indian Ocean Basin. *Marine Geology*, 158: 15–25.
- Iyer, S. D., Mascarenhas-Pereira, M. B. L., and Nath, B. N., 2007. Native aluminium (spherules and particles) in the Central Indian Basin sediments: Implications on the occurrence of hydrothermal events. *Marine Geology*, 240: 177–184.

Iyer, S. D., Amonkar, A., and Das, P., 2018. Genesis of Central Indian Ocean Basin Seamounts: Morphological, Petrological, Geochemical Evidence. *International Journal of Earth Science*. Doi: <https://doi.org/10.1007/s00531-018-1612-z>.

Kalangutkar, N.G., Iyer, S.D., Mascarenhas-Pereira, M.B.L. and Nath, B.N., 2015. Hydrothermal signature in ferromanganese oxide coatings on pumice from the Central Indian Ocean Basin. *Geo-Marine Letters*, 35: 221–235.

Kamesh Raju, K.A., 1993. Magnetic lineations, fracture zones and seamounts in the Central Indian Basin. *Marine Geology*, 109: 195–201.

K. A. Kamesh Raju; T. Ramprasad, V. N. Kodagali and R. R. Nair, 1993. Multibeam bathymetric, gravity and magnetic studies over 79°E fracture zone, Central Indian Basin. *J. Geophys. Res. (Solid Earth)*, 98, 9605-9618. <https://doi.org/10.1029/92JB01266>

Kleinman, B., 1969. Magnetite bearing spherules in tektites. *Geochimica et Cosmochimica Acta*, 33: 1,113–1,120.

Kodagali, V.N., KameshRaju, K.A., Ramprasad, T., George, P., and Jaishankar, S., 1992. Detailed bathymetric surveys in the Central Indian Basin. *International Hydrographic Review*, 69: 143–150.

Lefevre, R., Gaudichet, A., and Billon-Galland, M.A., 1986. Silicate microspherules intercepted in the plume of Etna volcano. *Nature*, 322: 817–820.

Lozovaya, N.G., 1981. Spherules in the bottom sediments of the Atlantic Ocean. *Oceanology*, 21: 60–65.

Ma, X.P., and Bai, S.L., 2002. Biological, depositional, microspherule, and geochemical records of the Frasnian/Famennian boundary beds, South China. *Palaeogeography, Palaeoclimatology, Palaeoecology*, 181: 325–346.

Mathur, S., Tripathi, R. P., Mathur, S. C., and Gaur, S. D., 2019. Implication from chemical study of magnetic spherules from a thin ferruginous layer located in Fatehgarh Formation of Barmer Basin, India. *Journal of the Geological Society of India*, 93: 56–60.

McCabe, C., Van der Voo, R., Peacor, D.R., Scotese, C.R., and Freeman, R., 1983. Diagenetic magnetite carries ancient yet secondary remanences in some Paleozoic sedimentary carbonates. *Geology*, 11: 221–223.

Melson, W.G., O'Hearn, T., and Friedrichson, K., 1988. Composition and origin of basaltic spherules in pelagic clay from the Eastern Pacific. *Marine Geology*, 83: 253–271.

Mukhopadhyay, R., Ghosh, A.K. and Iyer, S.D., 2018. The Indian Ocean nodule field: Geology and Resource Potential. 2nd edition. Elsevier, Amsterdam, 413.

Murray, J., and Renard, A., 1891. Report on Challenger expedition, 4, 327.

Mutch, T.A., 1966. Abundances of magnetic spherules in Silurian and Permian salt samples. *Earth Planetary Science Letters*, 1: 325–329.

Nashlund, H.R., Officer, C.B., and Johnson, G.D., 1986. Microspherules in Upper Cretaceous and Lower Tertiary clay layers at Gubbio, Italy. *Geology* 14: 923–926.

- Nath, B.N., Rao, V.P.C., and Becker, K.P., 1989. Geochemical evidence of terrigenous influence in deep-sea sediments upto 8°S in the Central Indian basin. *Marine Geology*, 87: 301–313.
- Nath, B.N., Borole, D.V., Aldahan, A., Patil, S.K., Mascarenhas–Pereira, M.B.L., Possnert, G., Ericsson, T., Ramaswamy, V., and Gupta, S.M., 2008. ^{210}Pb , ^{230}Th , and ^{10}Be in Central Indian Basin seamount sediments: Signatures of degassing and hydrothermal alteration of recent origin. *Geophysical Research Letters*, 35: L09603, doi:10.1029/2008GL033849.
- Nath, B.N., Sijinkumar, A.V., Borole, D.V., Gupta, S.M., Mergulhao, L.P., Mascarenhas- Pereira, M.B.L., Ramaswamy, V., Guptha, M.V.S., Possnert, G., Aldahan, A., Khadge, N.H., and Sharma, R., 2013. Record of carbonate preservation and the Mid-Brunhes climatic shift from a seamount top with low sedimentation rates in the Central Indian Basin. *Boreas*, 42: 762–778.
- Parthasarathy, G., Pandey, O.P., Sreedhar, B., Sharma, M., Tripathi, P., and Vedanti, N., 2019. First observation of microspherule from the infratrappean Gondwanasediments below Killari region of Deccan LIP, Maharashtra (India) and possible implications. *Geoscience Frontiers*, <https://doi.org/10.1016/j.gsf.2019.04.005>
- Pattersson, H., and Fredriksson, K., 1958. Magnetic spherules in Deep-sea deposits. *Pacific Science*, XIII: 71-81.
- Peckover, R.S., Buchanan, D.J., and Ashby, D.E., 1973. Fuel-coolant interactions in submarine volcanism. *Nature*, 245: 307–308.
- Puffer, J.H., Russell, E.W., and Rampino, M.R., 1980. Distribution and origin of magnetite spherules in air, waters, and sediments of the greater New York City area and the North Atlantic ocean. *Journal of Sedimentary Research*, 50: 247–256.
- Reshma, K., Rudraswami, N.G., and Prasad, M.S., 2013. Chondrule-like object from the Indian Ocean cosmic spherules. *Journal of Earth System Science*, 4: 1,161–1,171.
- Robin, E., Swinburn, N.H.M., Froget, L., Rocchia, R., and Gayraud, J., 1996. Characteristics and origin of the glass spherules from the Paleocene flood basalt province of western Greenland. *Geochimica et Cosmochimica Acta*, 60: 815–830. doi.org/10.1016/0016-7037(95)00433-5.
- Sarma, N.S., Kiran, R., Rama Reddy, M., Iyer, S.D., Peketi, A., Borole, D.V., and Krishna, M.S., 2018. Hydrothermal alteration promotes humic acid formation in sediments: A case study of the Central Indian Ocean Basin. *Journal of Geophysical Research: Oceans*, 123: 110–130. <https://doi.org/10.1002/2017JC012940>
- Schmidt, R.A., and Keil, K., 1966. Electron microprobe study of spherules from Atlantic Ocean sediments. *Geochimica et Cosmochimica Acta*, 30: 471–478.
- Sheridan, M.F., and Wohletz, K.H., 1981. Hydrovolcanic explosions, the systematics of water-tephra equilibration. *Science*, 212: 1,387–1,389.
- Shetye, S.S., Rudraswami, N.G., Nandakumar, K., and Manjrekar, S., 2019. Anthropogenic spherules in Zuari estuary, south west coast of India. *Marine Pollution Bulletin*, 143: 1–5.
- Shterenberg, L.E., Kuzmina, O.V., Laputina, I.P., and Tzepin, A.I., 1986. On the find of native aluminium in association with ZnO and ZnCl₂ in the sediments of site 647 (North-Eastern Pacific Ocean). *Lithology of Ore Deposit*, 1: 137–140 (in Russian).

- Suk, D., Van Der Voo, R and Peacor, D.R., 1990. Scanning and transmission electron microscope observations of magnetite and other iron phases in Ordovician carbonates from East Tennessee. *Journal of Geophysical Research*, 95: 12,327–12,336.
- Szoor, Gy., Elekes, Z., Rozsa, P., Uzonyi, I., and Simulaka, A.Z.K., 2001. Magnetic spherules: Cosmic dust or markers of a meteoritic impact? *Nuclear Instruments and Methods in Physics Research Section B: Beam Interactions with Materials and Atoms*, 181: 557-562.
- Von der Borch, C.C., and Rex, R.W., 1970. Amorphous iron oxide precipitates in sediments cored during Leg 5, Deep Sea Drilling Project. *Initial Report DSDP 5*: 541–544.
- Wang, K., and Chatterton, B.D.E., 1993. Microspherules in Devonian sediments: origin, geological significance, and contamination problems. *Journal of Earth Science*, 30: 1,660–1,667.
- White, J.D., 1996. Impure coolants and interaction dynamics of phreatomagmatic eruptions. *Journal of Volcanology and Geothermal Research*, 74: 155–170.
- Wohletz, K.H., 1983. Mechanisms of hydrovolcanic pyroclast formation: size, shape, and experimental studies. *Journal of Volcanology and Geothermal Research*, 17: 31–63.
- Wohletz, K.H., and McQueen, R.G., 1984a. Volcanic and stratospheric dustlike particles produced by experimental water-melt interactions. *Geology*, 12: 591–594.
- Wohletz, K.H., and McQueen, R.G., 1984b. Experimental studies of hydromagmatic volcanism. In: Boyd, Jr., F.R. (Ed.), *Explosive Volcanism; Inception, Evolution, and Hazards. (Studies in Geophysics.)* Natl. Academy Press, Washington, DC, 158–169.
- Wohletz, K.H., McQueen, R.G., and Morrissey, M., 1995. Experimental study of hydrovolcanism by fuel-coolant interaction analogs. In: *A multidisciplinary international seminar on intense multiphase interactions, Proceedings of US and Japan Joint Seminar*, 3-13: 287–317.
- Wright, F.W., and Hodge, P.W., 1965. Studies of particles for extraterrestrial origin. 4. Microscopic spherules from recent volcanic eruptions. *Journal of Geophysical Research*, 70: 3,889–3,898.
- Wu, Y., Sharma, M., LeCompte, M.A., Demitroffc, M.N., and Landisa, J.D., 2013. Origin and provenance of spherules and magnetic grains at the Younger Dryas boundary. www.pnas.org/cgi/doi/10.1073/pnas.1304059110
- Yatheesh, V., Dyment, J., Bhattacharya, G.C., Royer, J.Y., Kamesh Raju, K.A., and Ramprasad, T., 2019. Detailed structure and plate reconstructions of the Central Indian Ocean between 83.0 and 42.5 Ma (Chronos 34 and 20). *Journal of Geophysical Research. SolidEarth*, 124. <https://doi.org/10.1029/2018JB016812>
- Zagurskii, A.M., Ivanov, A.V., and Shoba, S.A., 2009. Submicromorphology of soil magnetic fractions. *Mineralogy and Micromorphology of Soils*, 42, 2: 1,044–1,052.
- Zhang, R. J., Zhang, H., Yao, H. Z., Wang, J. X., and Niu, Z. J., 2010. Microspherules found from the Upper Devonian limestone of Hainan Island. *Science Technology and Engineering*, 10: 8,123–8,127 (in Chinese with English abstract).

Zhang, W. H., Shi, X. Y., Tang, D. J., and Jiang, G. Q., 2014. Oncolites from Lower-Middle Cambrian transition of the western North China platform: A study of their ultra-fabrics and biomineralization. *Geoscience*, 28: 1–15.

Zimanowski, B., G. Fröhlich, and Lorenz, V., 1995. Experiments on vapour explosions by interaction of water with silicate melts, *Nuclear Engineering and Design*, 155: 335–343.

Zimanowski, B., Buttner, R., Lorenz, V., and Hafele, H., 1997. Fragmentation of basaltic melt in the course of explosive volcanism. *Journal of Geophysical Research*, 102: 803–814.

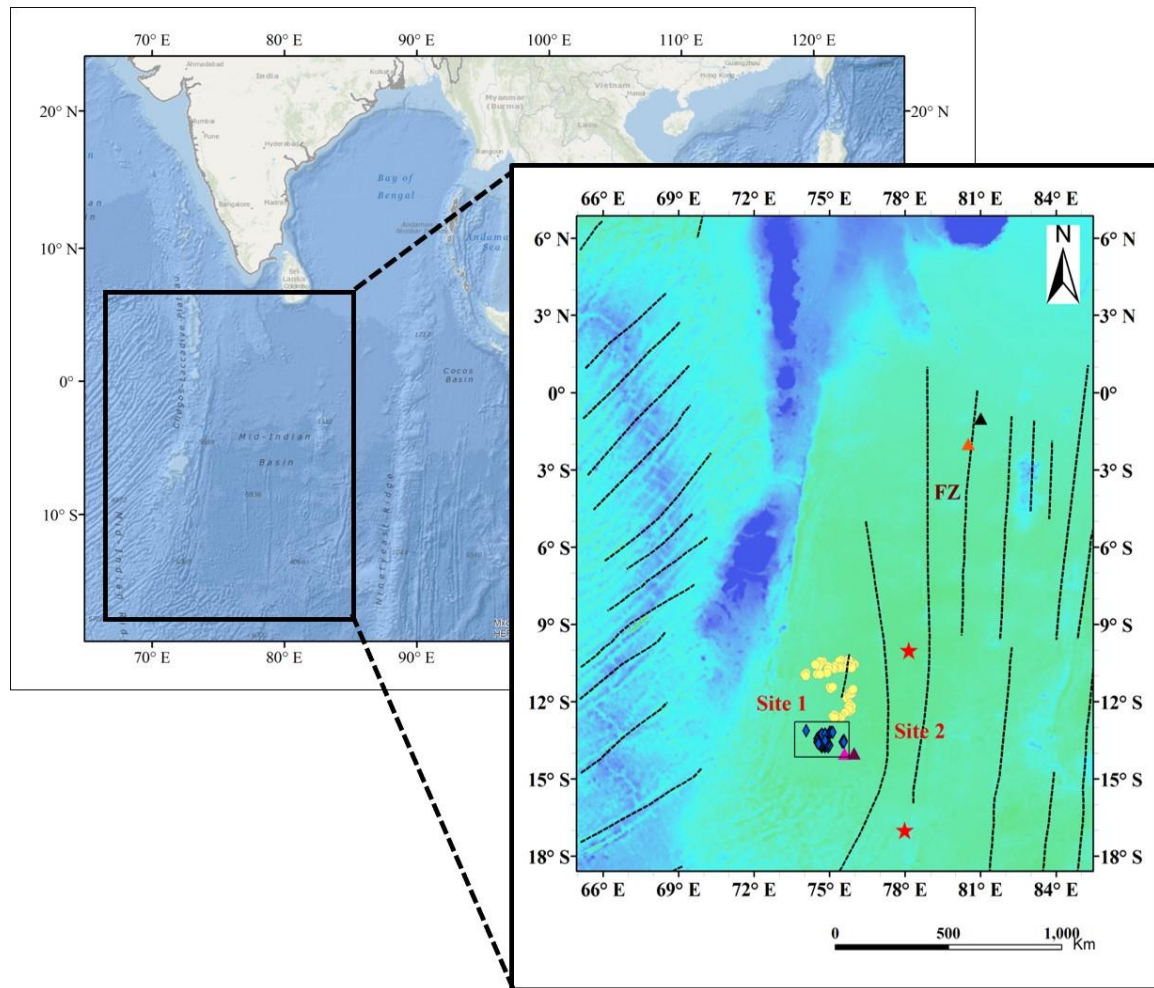


Figure 1: (A) Location of the study area in the CIOB. The yellow solid circles represent 55 locations and blue diamond inside a black outline box represents 40 locations. These 40 locations are referred to as Site-1. The red star symbol is the location of the gravity cores (AAS-22/7 (north) and AAS-22/3 (south) referred to as Site-2. The pink solid triangle represents SS2/89 (Iyer et al., 1997a), Purple solid triangle represents SS10/657 (Iyer et al., 1997a), the black solid triangle represents ODP Site 717-719 (Boulegue and Mariotti, 1990) and the red solid triangle represents SK-212 (Sarma et al., 2018). The map is created using data set from www.gebco.net

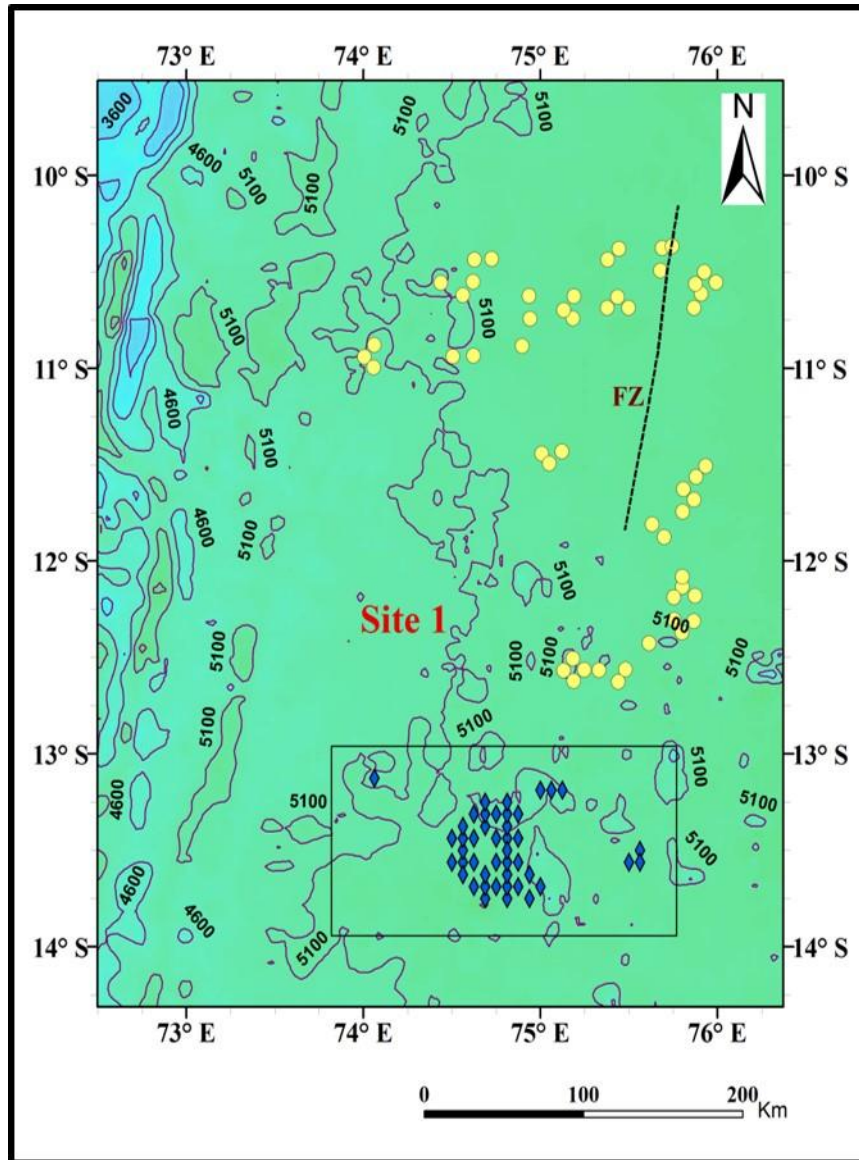


Figure 1: (B): Detailed map of study area (Site-1).

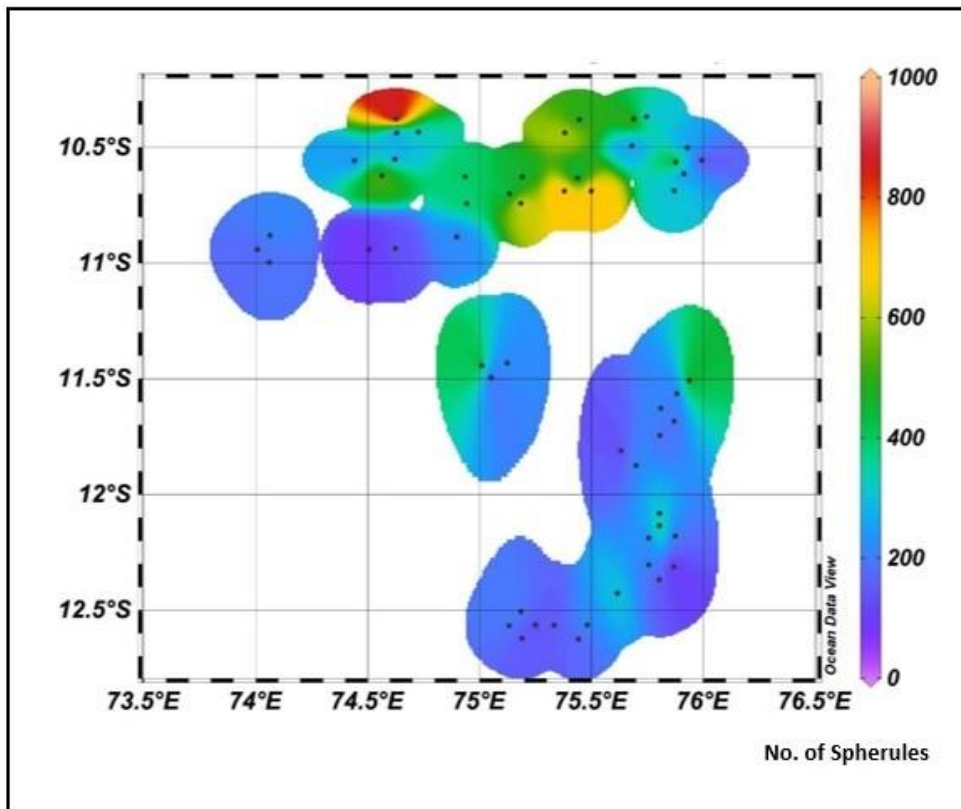


Figure 2: Spatial distribution of Fe-rich spherules from 55 locations within the CIOB. The vertical scale represents the number of spherules from 0 to 1000.



Figure 3: Photograph of baked sediment from depth 280-355 cm-bsf, core AAS-22/7.

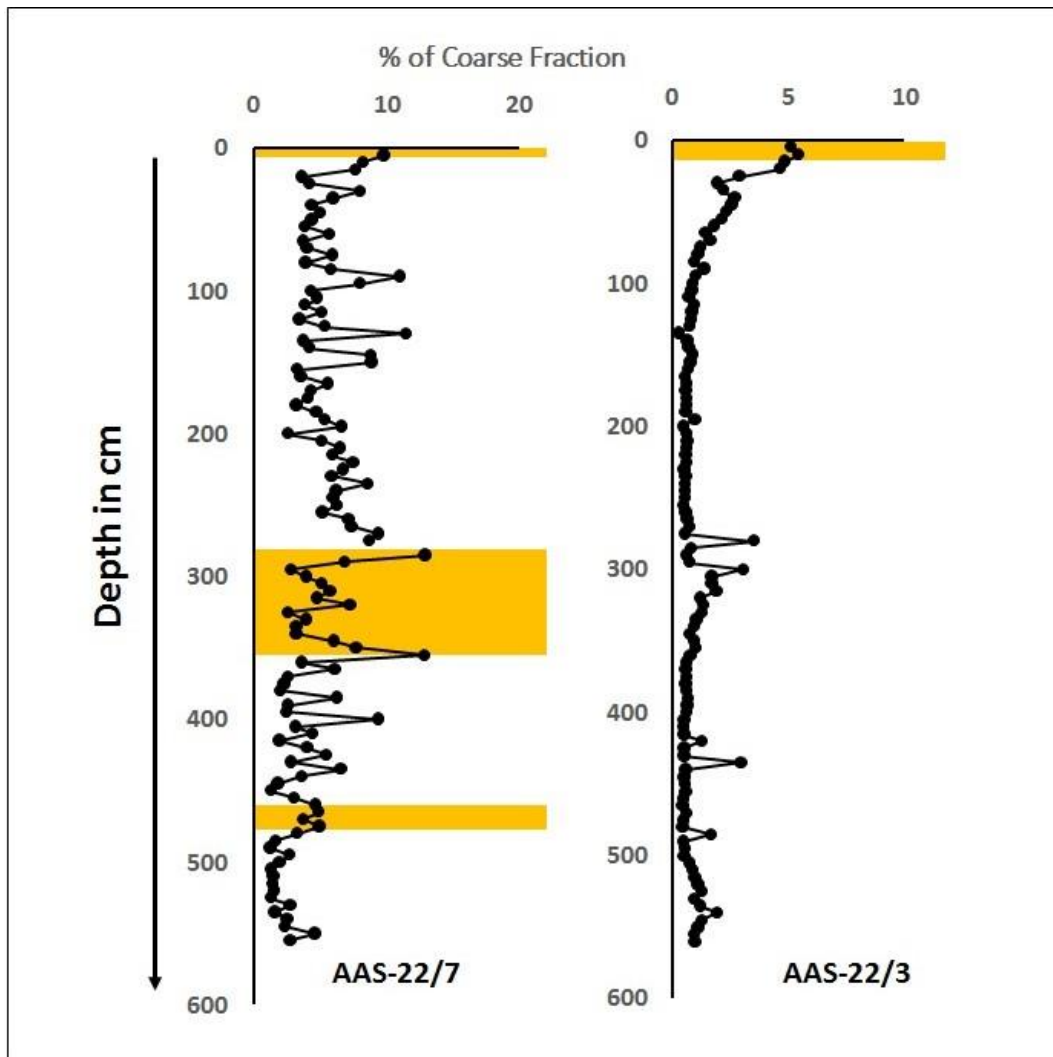


Figure 4: Represents the down core variation of $>63 \mu\text{m}$ fraction percentage in two studied cores from Site-2 of the CIOB. AAS-22/7 is the northern core while, core AAS-22/3 is located at the southern part of the basin. The yellow highlighted region indicates the depth of occurrence of spherules and Fe-rich particles.

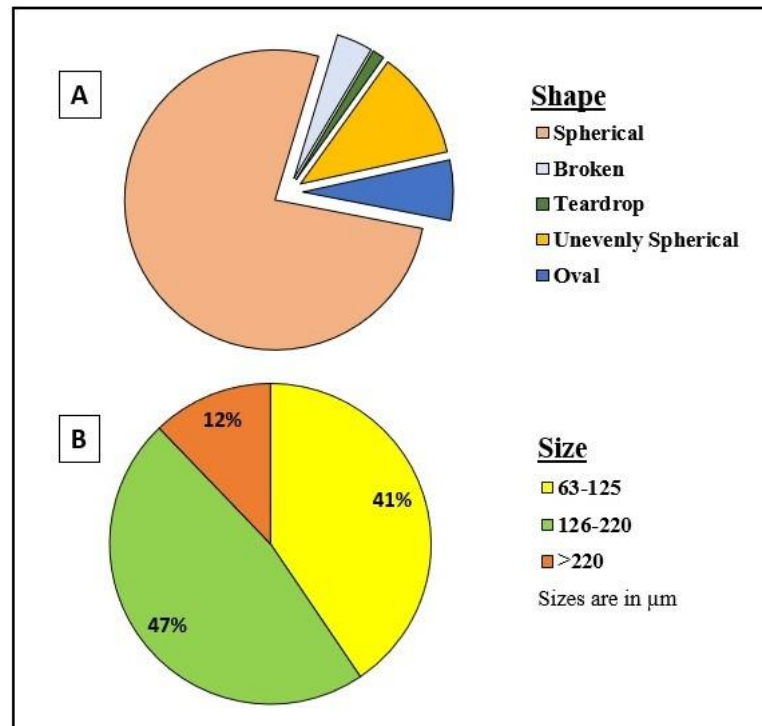


Figure 5A: The pie chart depicts the classification of Fe-rich spherules based on shape. The data are shown Table 2.

Figure 5B: The pie portrays the classification of Fe-rich spherules based on size. Spherules from the study area have been categorized into three different size range i.e. 63-125 μm, 126-220 μm, and >220 μm. The data used for this classification are detailed in Table 2.

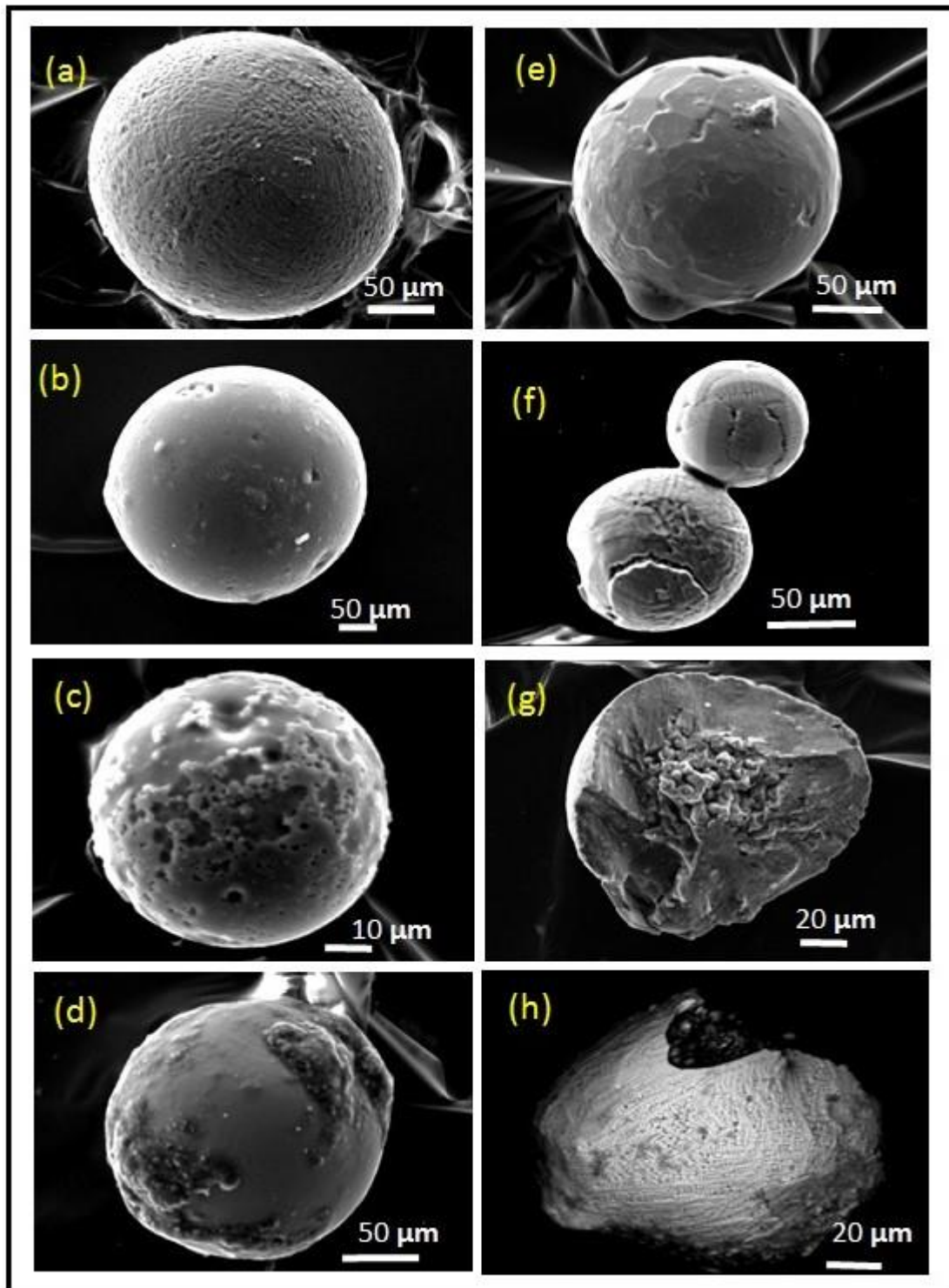


Figure 6: Scanning electron micrographs of type 1: Smooth spherules with no crystallinity (a, b), smooth spherules with surface aggregates (c, d), protruding tail (e), fused spherule (f) and broken spherule (g, h).

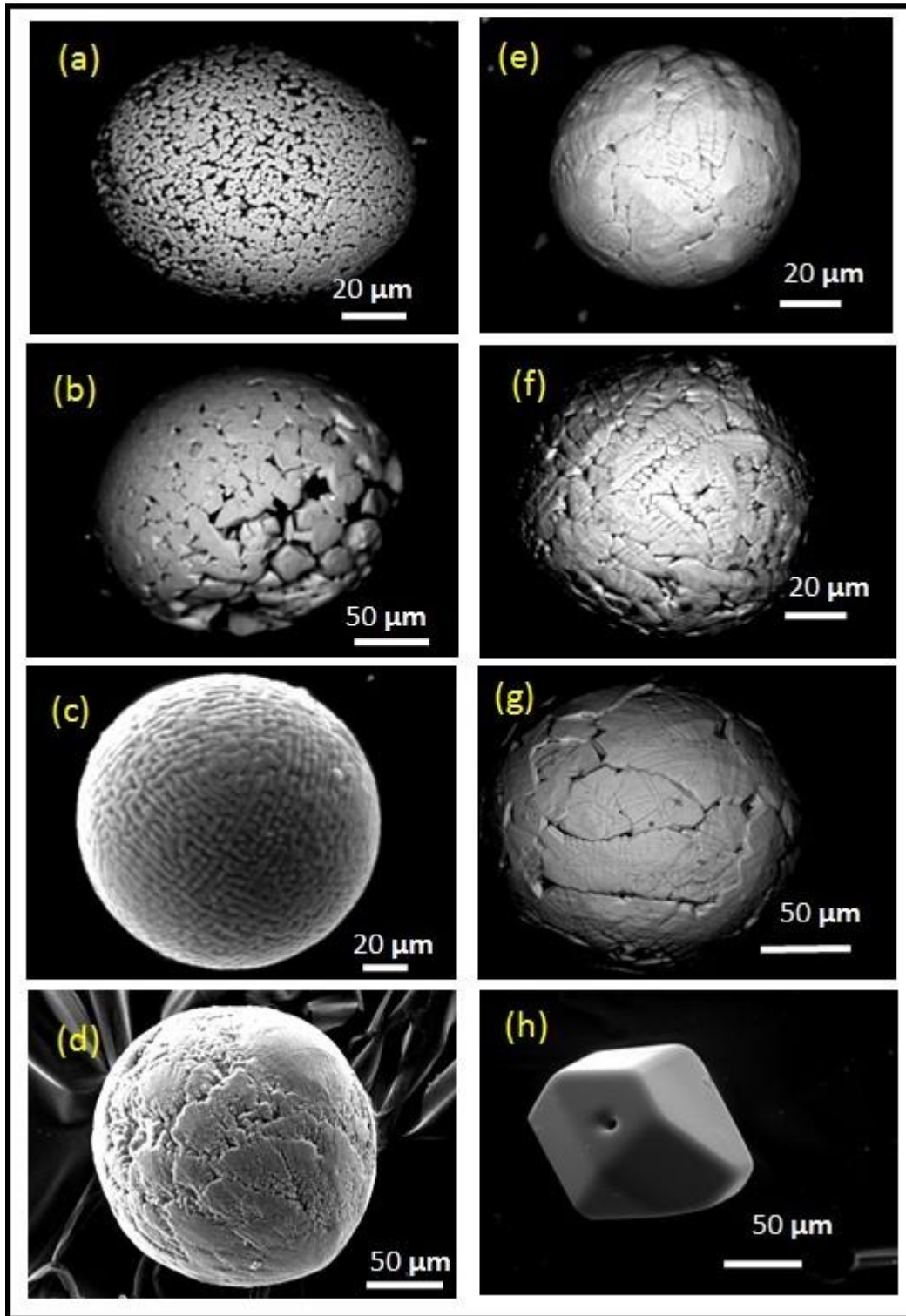


Figure 7: Scanning electron micrographs of type 2: textured spherules from the CIOB sediments. Brickwork (a,b), corkscrew (c), interlocking (d) and dendritic (e, f), blowholes between the interstices of crystals (g) and well-crystallized titano-magnetite grain (h).

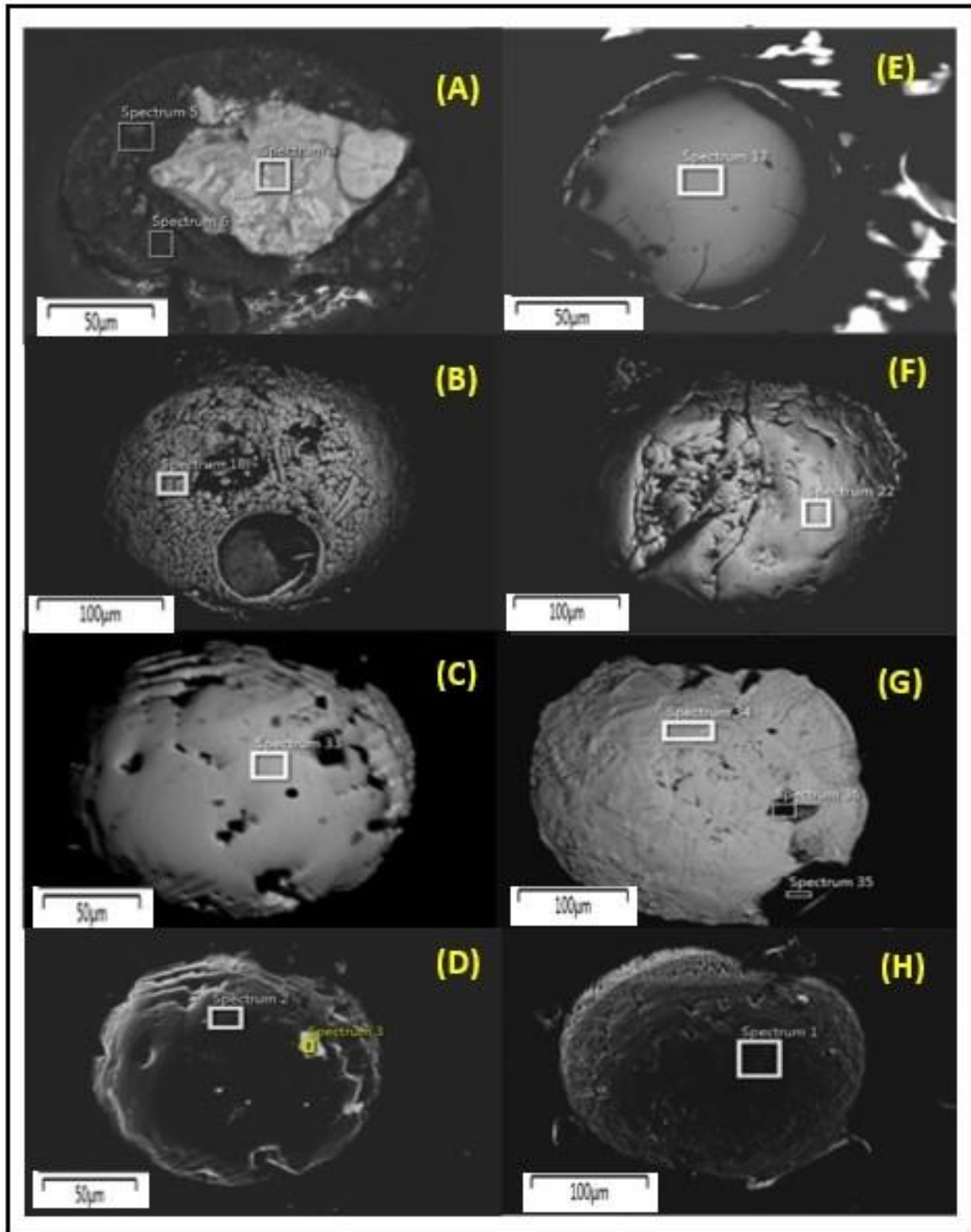


Figure 8: Scanning electron micrographs of polished spherules (A-H). The analysis was carried on different spots and is shown in a white rectangular box. The white aggregate in figures (A) is the isolation of Fe in silicate matrix, (B) magnetite crystals with a larger blowhole located in the lower side of the spherule, (C-H) do not show any characteristics in the interior.

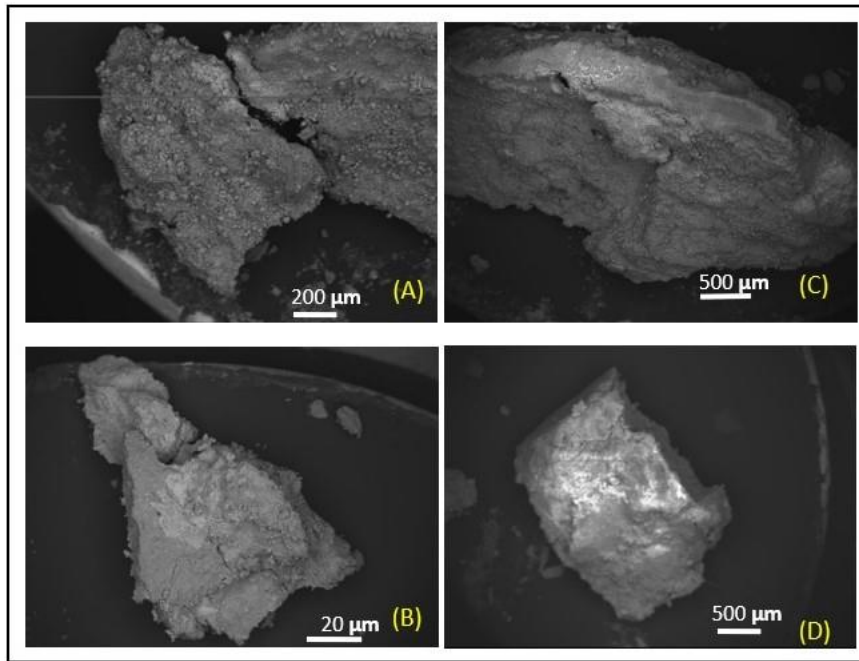


Figure 9: Scanning electron micrographs of Fe-rich particles that co-occur with Fe-rich spherules (A-D). These particles appear to be stubby and show fine granular texture.

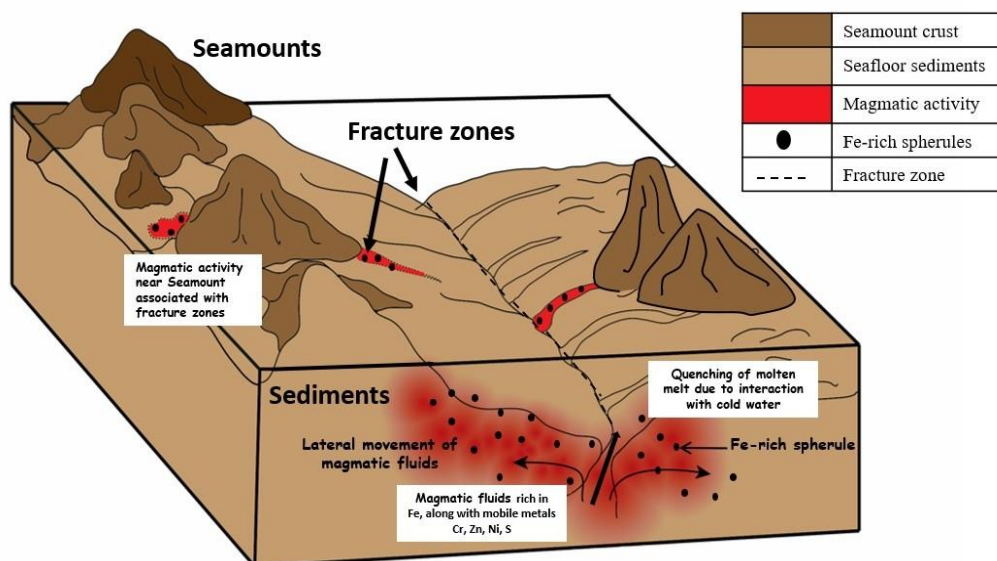


Figure 10: A schematic diagram of magmatic activity associated with fracture zone and seamounts and formation of spherules. Magmatic fluids of high temperature that are channelized along fractures and fissures undergo quenching on contact with cold seawater. Processes such as MFCI and hydrothermal exhalations are at play to produce Fe-rich spherules, basaltic clast and Fe-rich grains on the seafloor as well as within the sediments. The occurrence of such a mixture of pyroclast within the sediment cores is perhaps due to focused lateral movement of magmatic fluids.

Table 1A: Sampling location of surface sediments (55 stations) in the CIOB.

Sr. No	Station	Latitude °S	Longitude °E	Spherules
1	134	10.5003	75.9284	262
2	135	10.5552	75.9927	121
3	137	10.6123	75.9112	231
4	138	10.5622	75.8764	485
5	139	10.6852	75.8697	321
6	140	10.3758	75.6883	561
7	142	10.3667	75.7459	261
8	143	10.4921	75.6795	268
9	146	10.3796	75.4456	491
10	147	10.4353	75.3807	605
11	148	10.6299	75.4377	389
12	149	10.6866	75.4992	727
13	151	10.6862	75.3788	751
14	153	10.6255	75.1908	460
15	154	10.74	75.1847	672
16	155	10.6977	75.1336	388
17	156	10.625	74.9361	393
18	157	10.7425	74.9427	388
19	159	10.4323	74.7255	319
20	163	10.3759	7462.72	996
21	164	10.4356	74.6286	172
22	165	10.5494	74.6201	271
23	166	10.6208	74.5628	552
24	167	10.556	74.4393	241
25	168	10.8781	74.0625	223
26	169	10.9396	74.0066	167
27	170	10.9946	74.0591	186
28	172	10.938	74.506	86
29	173	10.8847	74.8972	218
30	175	10.9346	74.6224	145
31	177	11.4415	75.0089	533
32	178	11.4936	75.0507	85
33	179	11.4313	75.1239	227
34	180	11.8097	75.6323	126
35	182	11.8748	75.7001	224
36	185	11.6265	75.8103	242
37	186	11.7434	75.8056	165
38	187	11.6818	75.8696	156
39	188	11.5623	75.8808	161
40	189	11.5064	75.9359	541
41	191	12.1335	75.803	604

42	192	12.0806	75.8037	215
43	193	12.3684	75.8021	139
44	194	12.311	75.8671	29
45	195	12.1794	75.8745	184
46	196	12.1876	75.755	168
47	197	12.3035	75.7561	213
48	198	12.4261	75.616	305
49	201	12.5622	75.481	241
50	202	12.6251	75.4411	156
51	203	12.5646	75.3315	154
52	204	12.563	75.2481	129
53	205	12.5053	75.1848	209
54	206	12.5662	75.1321	201
55	207	12.6216	75.1894	141

Table 1B: Sampling location of surface sediments (40 stations) in the CIOB.

Sr. No	Station	Latitude °S	Longitude °E	Water depth (m)
1	OG-001	13.74989	74.68777	5329
2	OG-002	13.74992	74.81276	5195
3	OG-003	13.74994	74.93778	5261
4	OG-005	13.68751	74.68777	5131
5	OG-006	13.6875	74.75024	5200
6	OG-007	13.68742	74.81275	5168
7	OG-008	13.68749	74.87526	5279
8	OG-010	13.68748	75.00024	5167
9	OG-011	13.62501	74.93779	5260
10	OG-012	13.62498	74.81278	5260
11	OG-013	13.62493	74.68780	5193
12	OG-014	13.62492	74.56274	5204
13	OG-015	13.56254	74.50024	5095
14	OG-016	13.56241	74.56276	5230
15	OG-018	13.56250	74.75025	5168
16	OG-019	13.56224	74.81278	5167
17	OG-020	13.56226	74.87536	5204
18	OG-021	13.49994	74.56275	5170
19	OG-022	13.43749	74.50027	5204
20	OG-023	13.43741	74.56260	5192
21	OG-024	13.43742	74.62510	5141
22	OG-025	13.43741	74.75009	5221
23	OG-026	13.43741	74.81259	5190
24	OG-027	13.43741	74.87510	5192
25	OG-028	13.37490	74.56259	5190
26	OG-029	13.37491	74.68760	5153
27	OG-030	13.37497	74.81264	5152
28	OG-032	13.31253	74.62528	5232
29	OG-033	13.31262	74.68777	5220
30	OG-034	13.31257	74.75027	4750
31	OG-036	13.24993	74.68783	5165
32	OG-037	13.2500	74.81273	5123
33	OG-039	13.12495	74.06271	5249
34	OG-040	13.18748	75.00027	5229
35	OG-041	13.18743	75.06276	5064
36	OG-043	13.50001	75.56270	5217
37	OG-044	13.56245	75.50024	5280
38	OG-045	13.56251	75.56276	5156
39	OG-047	13.62495	74.56276	5230
40	OG-048	13.50005	74.81275	5140

Table 2.1: Classification of Fe-rich spherules from Site-1 (Seamount) based on shape, size, texture and general description

Sr No	Specimen Id	Shape	Description	Size(μm)	Texture
1	S1_0003	Spherical	Spherical with large magnetite crystals	170	Brickwork
2	S1_0005	Spherical	Large and small crystals of magnetite	250	Brickwork
3	S1_0013	Spherical	Large crystals well arranged with presence of blow holes	267	Broken tile-like
4	S1_0014	Spherical	Large crystals arranged in an interlocking pattern	97	Corkscrew
5	S1_0018	Spherical	Large crystals on the surface	80	Smooth, Corkscrew
6	S1_0021	Spherical	Large crystals on the surface	163	Brickwork
7	S1_0023	Spherical	Small crystals on the surface	196	Smooth
8	S1_0024	Spherical	Large crystals arranged in an interlocking pattern	85	Corkscrew
9	S1_0026	Spherical	Large crystals arranged in an interlocking pattern	136	Corkscrew
10	S1_0027	Spherical	Small crystals closely arranged	86	Smooth
11	S1_0028	Spherical	Small crystals well arranged	103	Broken tile-like
12	S1_0029	Spherical	Large crystals on the surface well arranged	245	Brickwork
13	S1_0030	Spherical	Large crystals on the surface	275	Brickwork
14	S1_0031	Spherical	Small crystals covering the whole spherule	116	Smooth
15	S1_0032	Spherical	Large crystals of magnetite, well arranged	101	Corkscrew
16	S1_0034	Spherical	Small crystals covering the whole surface	215	Brickwork
17	S5_0081	Spherical	Small crystals with mineral aggregates on the surface	213	Corkscrew
18	S5_0082	Spherical	Small size spherule	120	Smooth
19	S3	Spherical	Surface is smooth with a few mineral aggregates	136	Smooth
20	S3-1	Spherical	Mineral aggregates on spherule S3-1	136	Smooth
21	S4	Spherical	Platelets of magnetite crystals with cork-screw like distortions	185	Dendritic
22	S5	Spherical	Brick-work arrangement of magnetite crystals	224	Brickwork
23	S6	Broken	Spherule was partly broken	nd	Dendritic
24	S6-1	Broken	Fe-rich protrusions in spherule S6	nd	Smooth
25	S7	Broken	Spherule has a smooth surface with blowhole	nd	Smooth
26	S8	Spherical	Rough surface with mineral aggregates on the surface	262	Smooth
27	S14	Teardrop	Smooth surface with a few mineral aggregates, small blob protruding from surface	192	Brickwork
28	S15	Spherical	Quench texture on the surface of a spherule.	184	Dendritic
29	S16	Spherical	Smooth surface with aggregates on it	177	Smooth
30	S16-1	Spherical	Mineral aggregates on a part of the spherule.	177	Smooth
31	S17	Spherical	Contains dendritic texture on the surface.	73	Dendritic
32	S19	Spherical	Platelets of magnetite crystals with cork-screw-like distortions.	87	Cork-screw
33	S20	Spherical	Smooth surface with minor cracks	150	Smooth
34	S21	Spherical	Euhedral magnetite crystals are present	120	Dendritic
35	S22	Spherical	Blowholes are abundant on surface of spherule	71	Moss-like -
36	S23	Spherical	Two spherules are fused together	82	Cork-screw
37	S24	Spherical	Spherule contains blowholes and brickwork like texture.	97	Brickwork
38	S1_0103	Spherical	Large magnetite crystals on the surface of spherule	54	Brickwork

Table 2.2: Classification of Fe-rich spherules from Site-2 (Fracture Zone) based on shape, size, texture and general description.

Sr No	Sample Id	Shape	Description	Size(μm)	Texture
39	F_S251	Spherical	Smooth surface with few blowholes	125	Smooth
40	F_S27	Spherical	Surface contains platelets of larger crystals	207	Brickwork
41	F_S28	Spherical	Small crystals well arranged	189	Broken tile
42	F_S29	Spherical	Well-developed euhedral crystals on the surface	207	Brickwork
43	F_S30	Spherical	Surface is smooth with a few blowholes	85	Smooth
44	F_S311	Spherical	Surface is smooth, contains many blowholes and vesicles	234	Smooth
45	F_S32	Spherical	Euhedral crystals with few blowholes	136	Brickwork
46	F_S33	Spherical	Subhedral crystals with blowholes	72	Smooth
47	F_S34	Spherical	Rough surface and has several blowholes	98	Smooth
48	F_S35	Unevenly Spherical	Smooth surface with a few blowholes and cracks	79	Smooth
49	F_S361	Spherical	Tiny magnetite crystals with interlocking texture	219	Quenched
50	F_S37	Unevenly Spherical	Surface contains blowholes and accretion of minerals	170	Brickwork
51	F_S38	Oval	Smooth surface with a few blowholes	71	Smooth
52	F_S39	Spherical	Platelets of magnetite crystals with blowholes and cracks	167	Corkscrew
53	F_S40	Oval	Smooth surface with few blowholes	74	Smooth
54	F_S41	Oval	Oval in shape with smooth surface	62	Smooth
55	F_S42	Unevenly Spherical	Smooth surface with a few blowholes	72	Smooth
56	F_S43	Spherical	Spherical with a few blowholes	110	Smooth
57	F_S44	Unevenly Spherical	Unevenly spherical with a few blowholes.	140	Corkscrew
58	F_S451	Unevenly Spherical	Unevenly spherical with subhedral crystals and contains a lot of blowholes	255	Dendritic
59	F_S46	Spherical	Platelets of magnetite crystals	216	Brickwork
60	F_S471	Unevenly Spherical	Contains a few aggregates and blowholes on the surface	139	Corkscrew
61	F_S472	Unevenly Spherical	Spherical with a few blowholes	139	Corkscrew
62	F_S48	Unevenly Spherical	Rough surface with a few blowholes.	261	Dendritic
63	F_S50	Spherical	Smooth surface with a few aggregates.	105	Smooth
64	F_S51	Spherical	Euhedral magnetite crystals, smooth surface with a few blowholes	179	Corkscrew
65	F_P21	Spherical	Contains blowholes and crystal growth	118	Brickwork
66	F_P71	Spherical	Spherule with a small spherule attached to it.	390	Corkscrew
67	F_P81	Unevenly spherical	Uneven spherule with rough surface. Crystals are clearly visible.	138	Dendritic
68	F_P91	Oval	Rough surface with uneven bands of grey and white colour	137	Corkscrew
69	F_P92	Oval	Oval in shape with ranged magnetite crystal	137	Corkscrew
70	F_P121	Spherical	Surface contains blowholes and some accretion of material	190	Broken tile
71	F_P131	Spherical	Blowholes are present on the spherule	101	Brickwork
72	F_P141	Spherical	Spherule contains an extra coating of Fe	101	Smooth
73	F_P151	Spherical	The aggregate of high Si and Fe was observed on the surface	285	Brickwork
74	F_P182	Spherical	Large crystals of magnetite on the surface	210	Brickwork
75	F_P201	Spherical	Spherule has blowholes and few aggregates. (Contains high Fe and high Na)	141	Brickwork
76	F_P322	Spherical	Bands on the surface were observed	111	Smooth
77	F_P481	Spherical	Contains small crystals of magnetite	155	Smooth

Table 3: Elemental composition (EDX) of major elements occurring in Fe-rich spherules from Site-1 (Table 3A) and from Site-2 (Table 3B).

Sr No.	Sample Id	Si	Ti	Al	Fe	Mn	K	Mg	Ca	Na	O	Total
1	S3	nd	nd	nd	74.01	nd	nd	nd	nd	0.1	25.12	99.22
2	S3-1	11.39	nd	4.63	80.73	nd	nd	nd	3.25	nd	nd	100
3	S4	nd	nd	nd	86.94	nd	nd	nd	nd	nd	13.06	100
4	S5	nd	nd	nd	62.04	0.4	2.6	1.1	nd	0.8	32.46	99.4
5	S6	nd	nd	nd	61.76	nd	nd	nd	nd	nd	33.52	95.28
6	S6-1	nd	nd	2.6	62.97	1.2	nd	1.6	0.2	0.5	29.43	98.5
7	S7	nd	nd	nd	65.69	1.51	nd	nd	nd	nd	31.23	98.43
8	S8	2.58	nd	2.27	77.11	nd	0.1	nd	nd	nd	17.72	99.78
9	S14	0.35	nd	nd	80.05	nd	nd	nd	nd	nd	19.6	100
10	S15	0.45	nd	nd	71.60	nd	nd	nd	nd	nd	27.95	100
11	S16	1.33	nd	nd	65.24	nd	nd	nd	nd	0.21	31.75	98.53
12	S16-1	0.41	nd	1.29	65.24	1.83	nd	nd	nd	nd	31.03	99.8
13	S17	0.4	nd	nd	61.08	nd	nd	nd	0.31	nd	33.34	95.13
14	S19	nd	nd	nd	72.11	nd	nd	nd	nd	nd	27.89	100
15	S20	nd	nd	nd	72.24	nd	nd	nd	nd	nd	27.76	100
16	S21	0.51	nd	nd	75.94	nd	nd	nd	nd	nd	23.55	100
17	S23	0.39	nd	nd	68.6	0.53	nd	nd	nd	nd	30.47	99.99
18	S24	nd	nd	nd	69.56	nd	nd	nd	nd	nd	30.44	100
19	S-KS2	nd	nd	nd	76.87	0.86	nd	nd	nd	nd	22.27	100
20	S-KS8	0.3	nd	nd	77.23	nd	nd	nd	nd	nd	22.47	100
21	S-KS2	nd	nd	0.4	69.43	nd	4.6	2.4	nd	0.9	22.25	99.98
22	S-KS3	0.86	nd	nd	70.56	0.65	nd	nd	nd	1.57	22.8	96.44
23	S-KS4	1.07	nd	0.49	75.24	nd	nd	nd	nd	nd	23.2	100
24	S-KS5	0.35	nd	0.55	76.32	nd	nd	nd	nd	nd	22.76	99.98
25	S-KS1	nd	nd	0.39	77.16	nd	nd	nd	nd	nd	22.45	100
26	S-K6S2	0.43	nd	nd	77.17	nd	nd	nd	nd	nd	22.4	100
27	S-K3S5	1.64	0.8	0.44	71.72	1.39	0.81	nd	nd	nd	23.2	100
28	S-K3S4	0.34	nd	nd	76.44	nd	nd	nd	nd	nd	22.47	99.25
29	S-K3S1	0.28	nd	nd	75.87	1.4	nd	nd	nd	nd	22.44	99.99
30	S-K6S1	0.4	nd	0.43	76.44	nd	nd	nd	0.5	nd	22.73	100.5
31	S-KA25	0.36	nd	0.3	75.31	0.4	nd	1.1	nd	nd	22.6	100.07
Site-1, Avg. 31		1.25	0.80	1.25	72.54	1.02	2.03	1.55	1.07	0.68	25.35	99.36
Std Dev		2.53	-	1.38	6.22	0.51	2.01	0.61	1.46	0.54	4.98	1.35

Sr No.	Sample Id	Si	Ti	Al	Fe	Mn	K	Mg	Ca	Na	O	Total
32	F-S25-1	nd	nd	0.72	76.48	nd	nd	nd	nd	0.1	22.63	99.93
33	F-S27	nd	nd	nd	77.73	nd	nd	nd	nd	nd	22.27	100
34	F-S28	0.64	nd	0.33	76.19	nd	nd	nd	nd	nd	22.84	100
35	F-S29	0.38	nd	nd	75.26	1.84	nd	nd	nd	nd	22.52	100
36	F-S30	0.41	nd	nd	75.22	1.01	nd	nd	0.08	nd	22.64	99.36
37	F-S31-1	nd	0.41	nd	71.06	nd	0.52	2.7	nd	2.1	22.19	98.98
38	F-S32	nd	nd	nd	77.19	0.54	nd	nd	nd	nd	22.27	100
39	F-S33	0.17	nd	nd	76.98	0.46	nd	nd	nd	nd	22.38	99.99
40	F-S34	nd	nd	0.77	76.6	nd	nd	nd	nd	nd	22.63	100
41	F-S35	nd	nd	0.15	77.31	nd	nd	nd	nd	nd	22.36	99.82
42	F-S36-1	1.92	nd	0.32	68.46	nd	nd	2.29	0.85	nd	24.33	98.17
43	F-S37	0.23	nd	nd	76.67	0.67	nd	nd	nd	nd	22.4	99.97
44	F-S38	0.24	nd	nd	76.3	0.63	nd	nd	nd	nd	22.48	99.65
45	F-S39	0.37	nd	nd	76.14	0.97	nd	nd	nd	nd	22.52	100
46	F-S40	0.26	nd	0.15	76.1	0.6	nd	0.1	0.05	nd	22.56	99.82
47	F-S41	nd	nd	nd	77.73	nd	nd	nd	nd	nd	22.27	100
48	F-S42	0.11	nd	nd	77.05	0.49	nd	nd	nd	nd	22.35	100
49	F-S43	0.28	nd	nd	76.66	0.61	nd	nd	nd	nd	22.45	100
50	F-S44	0.15	0.24	nd	76.06	nd	nd	nd	nd	nd	22.57	99.02
51	F-S45-1	nd	nd	0.52	76.50	0.47	nd	nd	nd	nd	22.51	100
52	F-S46	0.12	0.95	0.78	74.70	0.37	nd	nd	nd	nd	22.97	99.89
53	F-S47-1	0.09	0.20	0.3	75.30	0.30	nd	nd	nd	0.12	22.6	98.91
54	F-S47-2	1.06	0.23	1.47	60.47	nd	1.14	0.98	0.88	4.66	24.52	95.41
55	F-S48	0.24	nd	0.51	75.92	0.52	nd	nd	nd	nd	22.63	99.82
56	F-S50	0.15	0.27	0.48	75.26	nd	nd	nd	nd	nd	22.77	98.93
57	F-S51	0.6	nd	0.22	74.97	1.21	nd	nd	nd	nd	22.77	99.77
Site-2,Avg. 26		0.41	0.38	0.52	75.17	0.71	0.83	1.52	0.47	1.75	22.67	99.52
Std Dev		0.45	0.29	0.36	3.59	0.40	0.44	1.20	0.46	2.16	0.55	0.97

Table 3C: Minor elements (EDX) occurring in Fe-rich spherules from the study area, P= (S17*=0.35), S= (S16-1=1.68), (S47-2=0.82), Cu= (S-K3S3=0.79, S-K3S4= 0.73) (nd= not detected).

Sr No	Sample Id	Cr	S	Zn	Ni
1	S3	nd	nd	nd	0.88
2	S6	nd	nd	nd	4.73
3	S6-1	nd	nd	nd	7.59
4	S7	nd	nd	nd	3.08
5	S8	nd	nd	0.31	nd
6	S16*	0.43	nd	nd	nd
7	S16-1	nd	1.68	nd	nd
8	S17*	nd	nd	nd	4.52
9	S-KS2	nd	0.3	nd	7.79
10	S-KS3	nd	nd	3.57	nd
11	S-K3S4	nd	nd	nd	nd
12	S-K3S3	nd	nd	0.64	nd
13	F-S25-1	0.17	nd	nd	nd
14	F-S30	0.72	nd	nd	nd
15	F-S31-1	nd	nd	6.34	nd
16	F-S35	0.18	nd	nd	nd
17	F-S36-1	nd	0.11	nd	2.67
18	F-S38	0.33	nd	nd	nd
19	F-S40	0.32	nd	nd	nd
20	F-S44	0.99	nd	nd	nd
21	F-S47-1	0.92	nd	nd	nd
22	F-S47-2	0.68	0.82	0.56	nd
23	F-S50	0.92	nd	nd	nd
24	F-S51	0.13	nd	nd	nd

Table 4: Elemental composition (EPMA) of eleven polished Fe-rich spherules from the CIOB.

Sr. No	Sample Id	Si	Ti	Al	Cr	Fe	Mn	Mg	Ca	Na	K	P	Ni	Total
1	NIO-21-Fes_1	0.07	0.03	0.05	0.02	98.23	0.72	0.01	0.03	0.01	0.00	0.01	0.01	99.17
2	NIO-21-Fes_2	0.19	0.00	0.06	0.03	98.78	0.75	0.01	0.00	0.00	0.00	0.00	0.00	99.83
3	NIO-21-Fes_3	0.04	0.03	0.05	0.04	98.39	0.71	0.01	0.03	0.02	0.00	0.02	0.02	99.35
4	NIO-21-Fes_4	0.03	0.01	0.07	0.05	98.67	0.68	0.00	0.00	0.00	0.00	0.00	0.03	99.54
5	NIO-21-Fes_5	0.02	0.01	0.08	0.07	100.06	0.69	0.00	0.00	0.00	0.00	0.00	0.01	100.95
6	NIO-21-Fes_6	0.17	0.02	0.11	0.06	99.39	0.75	0.01	0.01	0.04	0.00	0.00	0.05	100.58
7	NIO-21-Fes_7	0.05	0.01	0.08	0.02	100.01	0.53	0.01	0.01	0.01	0.00	0.01	0.01	100.74
8	NIO-21-Fes8_1	0.16	0.04	0.03	0.22	100.48	0.39	0.04	0.00	0.01	0.01	0.02	0.05	101.44
	NIO-21-Fes8_2	0.21	0.03	0.03	0.23	98.21	0.44	0.01	0.00	0.01	0.00	0.02	0.01	99.18
	NIO-21-Fes8_3	0.28	0.04	0.02	0.19	99.53	0.40	0.00	0.00	0.01	0.00	0.00	0.00	100.46
	NIO-21-Fes8_4	0.18	0.04	0.02	0.23	100.50	0.39	0.01	0.01	0.00	0.00	0.01	0.03	101.41
	NIO-21-Fes8_5	0.16	0.04	0.02	0.21	100.43	0.38	0.00	0.01	0.00	0.00	0.00	0.00	101.24
	NIO-21-Fes8_6	0.17	0.04	0.02	0.22	99.59	0.37	0.00	0.00	0.01	0.02	0.00	0.02	100.45
	NIO-21-Fes8_rim	0.64	0.03	0.05	0.16	98.36	0.36	0.00	0.01	0.03	0.00	0.02	0.06	99.73
9	NIO-21-Fes9_core	0.03	0.00	0.02	0.01	99.11	0.59	0.03	0.00	0.01	0.00	0.00	0.00	99.79
	NIO-21-Fes9_core	0.02	0.02	0.01	0.02	99.58	0.62	0.02	0.00	0.00	0.01	0.00	0.00	100.28
	NIO-21-Fes9_core	0.01	0.00	0.01	0.00	100.03	0.55	0.03	0.01	0.00	0.00	0.00	0.02	100.66
	NIO-21-Fes9_rim	0.10	0.00	0.01	0.01	99.91	0.55	0.03	0.00	0.01	0.00	0.01	0.01	100.63
	NIO-21-Fes9_rim	0.06	0.00	0.01	0.00	99.95	0.54	0.03	0.01	0.00	0.00	0.00	0.03	100.63
	NIO-21-Fes9_rim	0.02	0.00	0.02	0.00	99.36	0.53	0.00	0.00	0.00	0.01	0.00	0.00	99.93
	NIO-21-Fes9_rim	0.02	0.00	0.01	0.00	99.43	0.57	0.03	0.00	0.00	0.00	0.00	0.03	100.09
	NIO-21-Fes10_core	0.81	0.00	0.02	0.02	99.14	0.86	0.03	0.00	0.00	0.00	0.01	0.05	100.94
10	NIO-21-Fes10_core	0.54	0.01	0.02	0.00	99.81	0.87	0.01	0.01	0.03	0.00	0.00	0.02	101.31
	NIO-21-Fes10_rim	0.44	0.00	0.02	0.02	99.62	0.80	0.02	0.01	0.00	0.01	0.00	0.02	100.96
	NIO-21-Fes10_rim	0.35	0.00	0.08	0.00	99.56	0.69	0.00	0.02	0.00	0.02	0.01	0.05	100.78
11	NIO-21-Fes11	0.03	0.05	0.24	0.01	99.56	0.29	0.01	0.01	0.00	0.00	0.00	0.03	100.24
	NIO-21-Fes11	0.04	0.06	0.05	0.00	99.23	0.33	0.02	0.00	0.03	0.00	0.00	0.02	99.78
	NIO-21-Fes11_core	0.04	0.05	0.05	0.02	99.89	0.34	0.01	0.01	0.02	0.00	0.01	0.03	100.48
	NIO-21-Fes11_rim	0.03	0.03	0.03	0.00	99.11	0.32	0.01	0.00	0.01	0.00	0.00	0.01	99.54
	NIO-21-Fes11_rim	0.10	0.03	0.14	0.02	100.01	0.28	0.02	0.01	0.01	0.00	0.00	0.04	100.65
	NIO-21-Fes11_rim	0.06	0.04	0.07	0.01	99.51	0.30	0.02	0.00	0.00	0.01	0.00	0.00	100.03

Table 5: Elemental composition (EDX) of Fe-rich particles that are associated with spherules. Zn= 2.47 wt% in 32.-1*, P= 0.17 wt % in 29-1*, V= 0.63 wt% in 31.-1 and 0.70 wt% in 16.-1, Pb= 0.96wt% in 25-1, Cr and Cu is 0.10 wt% in 16-1.

Sr No	Sample Id	Si	Ti	Al	Fe	Mn	K	Mg	Ca	Na	O	Total
1	16-1	4.77	12	2.2	47	0.82	0.2	1	0.4	0.76	30.47	99.62
2	17-1	0.2	7.27	0.4	67	0.6	nd	nd	nd	nd	23.8	99.27
3	23-1	1.06	7.82	1.85	59.98	0.6	nd	1.84	nd	nd	26.63	99.78
4	25-1	0.75	nd	0.39	74.73	nd	0.1	nd	0.18	0.3	22.76	99.21
5	28-1	0.19	2.24	0.62	73.59	nd	nd	nd	nd	nd	23.35	99.99
6	31-1*	0.43	7.32	2.08	61.44	nd	nd	1.66	nd	nd	26.43	99.36
7	32-2	0.26	2.02	0.66	73.42	nd	nd	nd	0.26	0.01	23.37	100.0
	Avg. 7	1.09	6.45	1.17	65.31	0.67	0.15	1.5	0.28	0.36	25.26	99.60
	Std Dev	1.65	3.78	0.83	10.04	0.13	0.07	0.44	0.11	0.38	2.77	0.33

Table 6: Chemical data of Fe-rich spherules compared with other occurrences. Sr. No. 1 = Present study: Average of 31 Fe- rich spherules from Seamount (avg. Zn = 1.51 wt.%), 2 = Present study: Average of 26 Fe-rich spherules from FZ (contains Avg. Zn = 3.45 wt.%), 3 = Average of 7 Fe particles, 4 = Average of 17 volcanic magnetite spherules from SS2/94 (Iyer et al., 1999), 5 = Average of 24 volcanic magnetite spherules from SS2/89 and SS10/657 (Iyer et al., 1997a), 6 = Average of 5 Ti-rich areas in SS2/89 spherules (Iyer et al., 1997a), 7 = Magnetite spherules, Mt. Etna, 8 = magnetite spherules, Mt. Lipari, 9 = magnetite spherules, Mt. Vesuvius, 10 = magnetite spherules, Mt. Bracciano (Del Monte et al., 1975), 11 = Volcanic spherule from MAR, 12= Average of 57 basaltic spherules from DSDP Site 32, NE Pacific Ocean (Melson et al.,1988), 13 = Large Fe-Al Sphere, experimental Products (Heikenand Wohletz, 1985), 14 = Small Fe-Al Sphere, experimental Products (Heikenand Wohletz, 1985), 15 = Blocky Fe Particle, experimental Products (Heiken and Wohletz, 1985), 16 = VFZ, Vityaz fracture zone basaltic microlapilli (Nath and Iyer, 1989).

Sr. No	Si	Ti	Al	Fe	Mn	Mg	Ca	Na	K	Cr	Ba	Ni	S
1	1.25	0.80	1.25	72.54	1.02	1.55	1.07	0.68	2.03	0.43	nd	4.77	0.99
2	0.41	0.38	0.52	75.17	0.71	1.52	0.47	1.75	0.83	0.54	nd	2.67	0.47
3	1.09	6.45	1.17	65.31	0.67	1.5	0.28	0.36	0.15	nd	nd	nd	nd
4	0.234	0.14	1.46	75.98	0.32	0.62	0.08	0.05	0.06	0.13	0.13	1.14	0.07
5	0.89	0.36	0.36	73.8	0.36	0.63	0.32	0.29	0.07	0.11	0.12	0.14	1.55
6	7.35	31.25	2.8	9.6	4.96	0.86	1.75	0.37	2.21	0.43	0.68	na	na
7	0.23	na	0.1	73.05	na	na	na	na	na	na	na	na	na
8	0.15	na	0.09	71.91	na	na	na	na	na	na	na	na	na
9	0.07	na	0.05	72.1	na	na	na	na	na	na	na	na	na
10	0.25	na	0.16	71.01	0.05	na	na	na	na	na	na	na	na
11	na	na	na	71.5	0.37	na	na	na	na	na	na	na	na
12	23.67	0.65	7.33	10.04	na	3.9	6.85	1.97	0.27	na	na	na	na
13	4.71	na	16.63	45.04	na	na	0.32	na	0.26	na	na	na	na
14	5.02	na	13.28	49.89	na	na	na	na	na	na	na	na	na
15	6.7	1.35	6.01	44.31	1.22	3.88	1.46	2.28	1.59	na	na	na	na
16	21.86	0.7	7.41	7.15	0.15	5.4	9.39	na	0.36	na	na	na	na